

High-throughput vertebrate total analysis/screening platform

by

Tsung-Yao Chang

B.S., Electro-Mechanical Engineering, National Sun Yet-sen University, 2005
M.S., Biomedical Engineering, National Taiwan University, 2007

Submitted to the Department of Electrical Engineering and Computer Science
in partial fulfillment of the requirements for the degree of

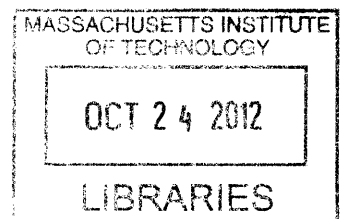
Doctor of Philosophy in Electrical Engineering

at the

MASSACHUSETTS INSTITUTE OF TECHNOLOGY

September 2012

ARCHIVES



© Massachusetts Institute of Technology 2012. All right reserved.

Author.....
Department of Electrical Engineering and Computer Science
August 30, 2012

Certified by.....
Mehmet Fatih Yanik
Professor of Electrical Engineering
Thesis Supervisor

Accepted by.....
Leslie A. Kolodziejcki
Professor of Electrical Engineering
Chairman, Department Committee on Graduate Theses

THIS PAGE IS INTENTIONALLY LEFT BLANK

High-throughput vertebrate total analysis and screening platform

by

Tsung-Yao Chang

Submitted to the Department of Electrical Engineering and Computer Science
on August 30, 2012,
in partial fulfillment of the requirements for the degree of
Doctor of Philosophy in Electrical Engineering and Computer Science

Abstract

High-throughput screening (HTS) is seen as one of the most promising technologies to facilitate biomedical studies and pharmaceutical discoveries. Although large varieties of *in vitro* HTS technologies have opened great opportunities, the speed of improvement has been limited by lack of advanced tools for *in vivo* screening on whole complex organisms, such as vertebrates. To address this issue, a high-throughput platform as a vertebrate total analysis/screening system (V-TAS) is proposed. This platform consists of two independent parts: an automated imaging system and an automated microinjection system. These two systems are designed for general high-content high-throughput pharmaceutical and genetic screens on whole zebrafish larvae, and therefore, are well-modularized for adapting different situations. Furthermore, to demonstrate the capability of V-TAS, a screen of lipidoid library for biologics delivery on thousands of animals was conducted. Very limited damage to the larvae was shown during the screening. In the end, the author also validated the hits discovered by V-TAS can be applied to more advanced animal models such as rats, and be more predictable than cell-based assays.

Thesis Supervisor: Mehmet Fatih Yanik

Title: Associate Professor of Electrical Engineering and Computer Science

Acknowledgements

I would like to express my deepest gratitude to my advisor, Dr. Mehmet Fatih Yanik, for his excellent guidance, caring, patience, and providing me with an excellent atmosphere for doing research. I would like to thank Dr. Hatice Altug, who let me experience the research of nanotechnology beyond the textbooks and patiently corrected my writing. I would also like to appreciate Dr. Louis Braida and Dr. Dennis Freeman for guiding my research for the past few years and helping me to develop my background.

I would like to specially thank Foxconn's founder and CEO, Mr. Terry Gou, who has supported me throughout my PhD with his mentoring, encouraging and funding. Without him, I would not have an opportunity to participate in such an exciting venture.

I also thank Chialing Pai and Chihyu Huang, who as my girlfriend and ex- girlfriend, were always willing to support and give their best suggestions. Many thanks to Peng Shi, Min Huang, Ali Yanik, Carlos Pardo, Joe Steinmeyer, Paul Tillberg and other co-workers in the laboratory of Dr. Yanik for helping me on different aspects in the research. My research would not have been possible without their helps.

Finally, I deeply appreciate and thank my whole family, my parents and my sister. They were always supportive with their best wishes and wisdom.

TABLE OF CONTENTS

Abstract.....	i
Acknowledgements	ii
Table of Contents	iii
Chapter 1: Background and Introduction	001
1-1 Introduction	001
1-2 Background	003
1-3 Chemical Screens of Zebrafish and High-throughput Platform	005
Figures	007
References	008
Chapter 2: Vertebrate Automated Screening Technology	010
2-1 Introduction and System Setup	010
2-2 System Performance	011
2-3 Hardware/Software Architecture and Operation	014
Figures	018
References	025
Chapter 3: Fully Automated Cellular Resolution Vertebrate Screening Platform with Parallel Processing	026
3-1 Introduction and System Setup	026
3-2 Multi-thread Operation	027
3-3 Fluorescence/bright Field Automated Larvae Discriminator	028

3-4	Identification of Zebrafish Orientation and Position	030
3-5	Analysis of Capillary Materials for High Quality Imaging	033
3-6	Conclusions.....	035
3-7	Algorithms and Software for Operation Sequence	036
	Figures	037
	References	044
 Chapter 4: Vertebrate Automated Microinjection System		045
4-1	Introduction	045
4-2	System Setup.....	047
4-3	Image Processing and Recognition.....	050
4-4	System Hardware Architecture	053
4-5	Health Assessment	054
	Figures	055
	References	060
 Chapter 5: Screenings: from Cells, Zebrafish to Rodents		062
5-1	Introduction	062
5-2	In vivo Screening of Zebrafish and Validation	063
5-3	Ventricle Injection in Rats	065
5-4	Rodent Primary Neural Cells	066
5-5	Lipidoids-mRNA Formulation	066
5-6	Dot-blot of Rodent Brain Tissues	067
	Figures	069

References	072
Chapter 6: Conclusions	073
6-1 Conclusions.....	073
References	076
Appendix A: CAC Protocol 0309-025-12 for Subcellular Imaging	077
Appendix B: CAC Protocol 0112-008-15 for Microinjection	089
Appendix C: CAC Protocol 1011-126-14 for Rodent Injection	100
Appendix D: Major Publications during Ph.D Studies	108

Chapter 1

Introduction and background

1-1 Introduction

The pharmaceutical industry is facing unprecedented productivity challenges in the recent years. Since 2000, the number of new drug approvals (NDA) by the FDA is significantly decreasing although the R&D expenditure in pharmaceutical companies has increased three-fold from 2000 to 2009 [1]. It is believed there is a huge need for novel methods for drug discovery in order to improve this situation. Among recent proposed methods, high-throughput screening (HTS) technologies are taking the lead because of their speed and cost-effective ratio [2].

HTS-based *in vitro* drug screening assays are widely applied to pharmaceutical companies because of the increasing number and diversity of compounds made available by rapid synthesis techniques such as combinatorial chemistry. However, validating these *in vivo* preliminary hits made by *in vitro* drug screening by mammalian animal models is slow and costly, resulting in a gap in the drug development process. The zebrafish is a vertebrate model organism that holds a great potential to bridge this gap [3-11]. In fact, zebrafish represent as one of the most ideal animal models for *in vivo* high-throughput screening [12, 13]. The trend of zebrafish studies is also growing exponentially.

Although zebrafish have many advantages over other animal models, crucial problems still exist. First of all, there are very limited automation systems proposed for this animal model. As an animal model known for its high-throughput potential, there is a significant need for developing automation systems to fulfill the potential of this model. For instance, researchers usually need to precisely orient and immobilize larvae in order to image or manipulate the animal at the cellular level. Current orientation control methods require embedding the sample in viscous media such as agar and manually orienting the fish with forceps. This process is slow and unreliable for high-throughput screens, which dramatically hinders the capability of high-throughput screening on the zebrafish. In addition, the samples cannot be rapidly re-oriented once they are fixed, thus impeding visualization of organs from multiple angles. Furthermore, manual manipulation of the animal can also increase the uncertainty and variation. Damage of the larvae can be often observed with incautious operations as well.

To address those issues, the author proposes an *in vivo* total analysis/screening platform (*in vivo*-TAP). *In vivo*-TAP consists of two individual systems: an automated subcellular imaging system [4, 5] and an automated microinjection system. This platform includes most of important functions needed for the *in vivo* screening pipeline on small animal model, such as sorting, subcellular imaging, high-precision orientation, injection etc. Currently, this platform has been setup [5]. The author further applied pipelining apparatus to

minimize the screening cycle [4]. In order to demonstrate the capability of this platform, the author has successfully performed a screen on a library of transfection reagents for neural cells and further validated the results via testing assays on rodent models.

1-2 Background

A one of the most suitable vertebrate animal models for microfluidic operations, zebrafish (*Danio Rerio*) facilitates the study of complex processes on a large scale that cannot be replicated in vitro such as: organ development; neural degeneration and regeneration; stem cell proliferation and migration; cardiovascular, immune, endocrine, and nervous system functions; infectious disease progression; pathogenesis; cancer progression; and tissue specificity and toxicity of drugs. Several desirable attributes of zebrafish have fueled its popularity, including the animal's small size, optical transparency, aquatic habitat, and simplicity of culture. Zebrafish models of several human diseases have been developed [11, 13-16]. Leading compounds discovered by screening chemical compound libraries for efficacy in zebrafish disease models have been useful for pharmaceutical discovery due to the high level of conservation of drug activity between mammals and zebrafish [9, 17-19]. The availability of large numbers of mutant strains and genetic manipulations such as gene overexpression, knockdown, and silencing make zebrafish a powerful model for genetic studies and for identification of the cellular targets of new compounds [9, 20]. The significant advantages of zebrafish have fueled

exponential growth of its use in experimental investigations over the last two decades.

Although zebrafish have so many advantages over other animal models, crucial problems still exist. For instance, researchers usually need to precisely orient and immobilize larvae in order to image the animal at the cellular level. Current orientation control methods require embedding the sample in viscous media such as agar and manually orienting the fish with forceps. This process is slow and unreliable for high-throughput screens, which dramatically hinders the capability of high-throughput screening on zebrafish. In addition, the samples cannot be rapidly re-oriented once they are fixed, thus impeding visualization of organs from multiple angles.

In order to address those issues, we demonstrate a platform for rapid manipulation of zebrafish larvae for high-throughput subcellular-resolution genetic and chemical screen. A complete cycle consisting of loading, positioning, rotating, sub-cellular resolution confocal imaging, and dispensing each animal takes less than 16 seconds. Screening hundreds of animals demonstrates that the system works noninvasively and reliably in the presence of artifacts such as air bubbles and debris in the growth medium.

On the other hand, except the need for a high-content and high-throughput imaging technology, injection technology on larvae for material delivery, gene modification and advanced toxicity assays etc. is a general and important technique in zebrafish animal model. Conventionally, researchers need to anesthetize, orient, immobilize with a suction tip and then inject

manually in order to deliver materials into the animal. The whole process usually takes 5-10 minutes. Although some researchers have demonstrated the automated high-throughput microinjection systems for zebrafish embryos [21], this kind of setup is mainly for material delivery or gene modification during the early embryonic stage (within 10 hours after fertilization), and therefore, have very limited applications. In order to achieve precise material delivery in vivo in high-throughput for wide applications, an automated microinjection technology for larvae is crucial. With this high-throughput in vivo microinjection technology, we can enable assays which are hard to achieve with current technologies, such as large-scale in vivo transfection reagent screenings, tissue-specific gene modification/transfection, advanced toxicity assays or cancer cell transplantation and so on.

To sum up, the goal of this work is to build a total analysis/screening high-throughput platform on a whole vertebrate organism for addressing the problems mentioned above. The author validated the capability of this platform with screening on drug libraries and further tested on rodent models.

1-3 Typical chemical screens of zebrafish and high-throughput platform

To facilitate a dramatic improvement in the throughput and complexity of zebrafish screens, we developed a platform for rapid manipulation of zebrafish larvae for imaging and injecting. The automated system allows both genetic and

pharmaceutical screens, as shown in **Fig. 1-2** Chemical screen: Animals are loaded from a reservoir to the imaging platform, which can be used either to count the number of animals and/or to perform optical manipulations such as laser microsurgery. The animals are then dispensed into multiwell plates containing chemicals to be tested. However, in many cases, chemicals either cannot penetrate through various endothelial tissue barriers such as blood-brain barrier [22], thus require to be injected to test drug efficacy and toxicity. Another general way to transfer chemicals/reagents is via microinjection of zebrafish larva and embryos. Microinjecting is a time-consuming process which usually takes 5-10 minutes for orienting, immobilizing, positioning and injecting of each larva. Our platform can facilitate microinjection via the automation of these processes in an innovative fashion. After incubation/microinjection within chemicals, the animals are loaded back into the imaging platform to check phenotypes.

Figures

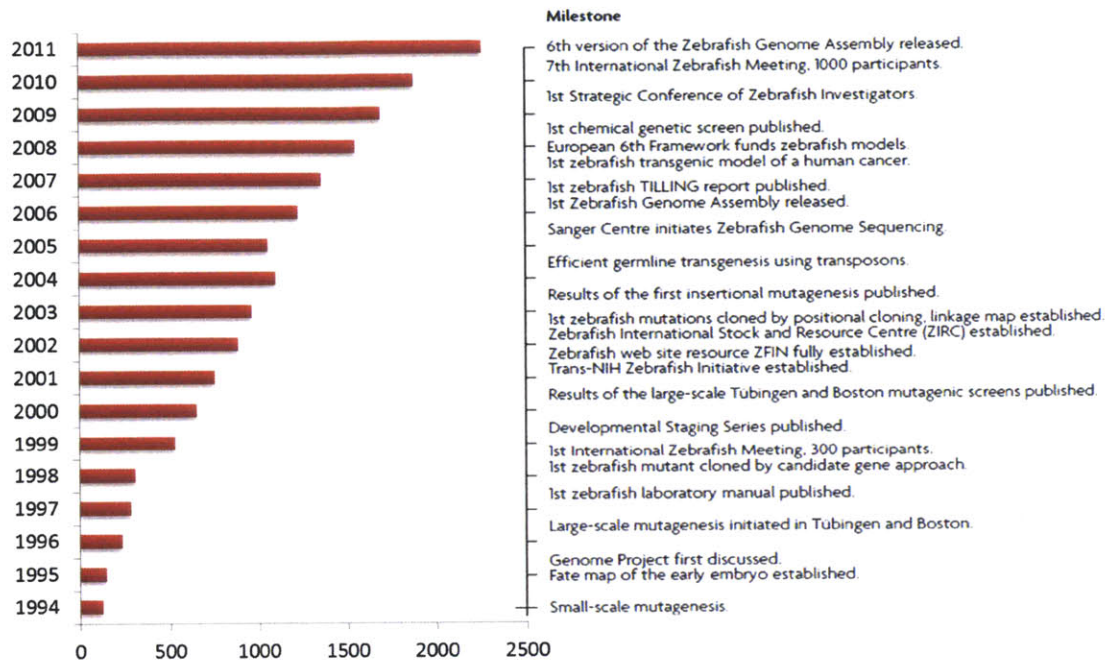


Figure 1-1. A historical perspective of zebrafish research.

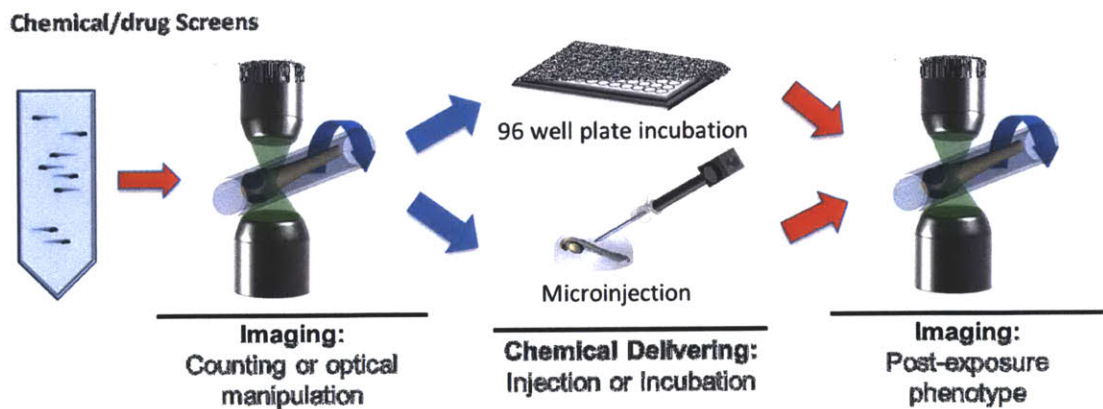


Figure 1-2. Flow diagram for chemical and drug screens from loading, imaging, material delivering to image for phenotyping.

References

1. Macarron, R., et al., *Impact of high-throughput screening in biomedical research*. Nat Rev Drug Discov, 2011. **10**(3): p. 188-95.
2. Mayr, L.M. and D. Bojanic, *Novel trends in high-throughput screening*. Curr Opin Pharmacol, 2009. **9**(5): p. 580-8.
3. Lieschke, G.J. and P.D. Currie, *Animal models of human disease: zebrafish swim into view*. Nat Rev Genet, 2007. **8**(5): p. 353-67.
4. Chang, T.Y., et al., *Fully automated cellular-resolution vertebrate screening platform with parallel animal processing*. Lab Chip, 2012. **12**(4): p. 711-6.
5. Pardo-Martin, C., et al., *High-throughput in vivo vertebrate screening*. Nat Methods, 2010. **7**(8): p. 634-6.
6. Sukardi, H., et al., *Zebrafish for drug toxicity screening: bridging the in vitro cell-based models and in vivo mammalian models*. Expert Opin Drug Metab Toxicol, 2011. **7**(5): p. 579-89.
7. Lam, S.H., et al., *Zebrafish whole-adult-organism chemogenomics for large-scale predictive and discovery chemical biology*. PLoS Genet, 2008. **4**(7): p. e1000121.
8. Brittijn, S.A., et al., *Zebrafish development and regeneration: new tools for biomedical research*. Int J Dev Biol, 2009. **53**(5-6): p. 835-50.
9. Barros, T.P., et al., *Zebrafish: an emerging technology for in vivo pharmacological assessment to identify potential safety liabilities in early drug discovery*. Br J Pharmacol, 2008. **154**(7): p. 1400-13.
10. Parng, C., et al., *Zebrafish: a preclinical model for drug screening*. Assay Drug Dev Technol, 2002. **1**(1 Pt 1): p. 41-8.
11. Rubinstein, A.L., *Zebrafish: From disease modeling to drug discovery*. Current Opinion in Drug Discovery & Development, 2003. **6**(2): p. 218-223.
12. Zon, L.I. and R.T. Peterson, *In vivo drug discovery in the zebrafish*. Nat Rev Drug Discov, 2005. **4**(1): p. 35-44.
13. Langheinrich, U., *Zebrafish: a new model on the pharmaceutical catwalk*. Bioessays, 2003. **25**(9): p. 904-12.
14. McGrath, P. and C.Q. Li, *Zebrafish: a predictive model for assessing drug-induced toxicity*. Drug Discov Today, 2008. **13**(9-10): p. 394-401.

15. Stoletov, K. and R. Klemke, *Catch of the day: zebrafish as a human cancer model*. *Oncogene*, 2008. **27**(33): p. 4509-20.
16. Kim, S.U. and J. de Vellis, *Stem cell-based cell therapy in neurological diseases: a review*. *J Neurosci Res*, 2009. **87**(10): p. 2183-200.
17. Jette, C.A., et al., *BIM and other BCL-2 family proteins exhibit cross-species conservation of function between zebrafish and mammals*. *Cell Death Differ*, 2008. **15**(6): p. 1063-72.
18. Kokel, D. and R.T. Peterson, *Chemobehavioural phenomics and behaviour-based psychiatric drug discovery in the zebrafish*. *Brief Funct Genomic Proteomic*, 2008. **7**(6): p. 483-90.
19. Zimmerman, J.E., et al., *Conservation of sleep: insights from non-mammalian model systems*. *Trends Neurosci*, 2008. **31**(7): p. 371-6.
20. Whitehead, K.A., R. Langer, and D.G. Anderson, *Knocking down barriers: advances in siRNA delivery*. *Nat Rev Drug Discov*, 2009. **8**(2): p. 129-38.
21. Wang, W., et al., *A fully automated robotic system for microinjection of zebrafish embryos*. *PLoS One*, 2007. **2**(9): p. e862.
22. Gabathuler, R., *Approaches to transport therapeutic drugs across the blood-brain barrier to treat brain diseases*. *Neurobiol Dis*, 2010. **37**(1): p. 48-57.

Chapter 2

Setup of *Vertebrate Automated Screening Technology (VAST)*

2-1 Introduction and System Setup

The automated system for vertebrate high-throughput screening allows both genetic and pharmaceutical screens. Specimens can be repositioned and rotated on the fly, eliminating the need for manual handling and 1-phenyl 2-thiourea (PTU) treatment. Each screening cycle of the machine comprises the following major steps: loading, detection, positioning, orienting and focusing, imaging, and dispensing (**Figure 2-1**).

During loading, the system extracts larvae either from a multiwell plate or a reservoir. Fluid is driven by a computer-controlled syringe pump. A high-speed photodetection system composed of a photodiode and two LEDs discerns the entry of larvae into the loading tube. The photodiode senses transmitted light from one LED and scattered light from the other LED. By simultaneously monitoring both the transmission and scattering signals, the system discriminates the passage of a larva from air bubbles and debris with 100% reliability ($n = 1000$). After loading and photodetection, the larva transits from the larger loading tube into an index-matched capillary within the field-of-view (FOV) of an optical

imaging and manipulation subsystem. The capillary has a refractive index similar to water, allowing the use of high numerical-aperture (NA) water-immersion objectives that require short working distances. Using a fast camera and an automated image processing algorithm, the larva is coarsely positioned by the syringe pump within the FOV. Next, a 3-axis stage automatically moves the capillary assembly so that the larva's head is precisely positioned to the center of the FOV. The larva is then rotationally oriented by a pair of stepper motors. Thus, larva can be arbitrarily positioned and oriented in the microscope's FOV. At the end of the screening cycle, animals can be dispensed back into either individual wells or larger containers by executing the loading process in reverse.

2-2 System Performance

The optical imaging and manipulation subsystem includes two microscope objectives; an upright, high-resolution water-immersion objective and an inverted air objective. This allows both wide-field fluorescence imaging and high-resolution confocal-microscopy. **Figure 2-2a** shows confocal images of a larva oriented at two different angles to visualize the midline crossing of the Mauthner motor neuron axons that project into spinal cord. The midline crossing is only visible when directly observed from the hindbrain (0° in the figure). At less favorable orientations, the structure is obscured. We performed an illustrative screen on a similar midline crossing of retinal axon projections to the optic tectum (**Figure 2-**

2b). This mutant screen had previously led to the discovery of *robo2* mutant with retinal axon misguidance [1]. Using our system, we were able to distinguish wild-types from mutants with a sensitivity of 100% and specificity of 98.8% for a 96-well plate with 83 randomly seeded mutants. Thus, this mutant screen can be used for large-scale pharmaceutical screens for discovery of small molecules that rescue such misguidance.

In conjunction with the sample positioning and orientation capability, the optical system also allows subcellular-precision laser manipulations such as localized activation of fluorescent reporters and ion channels, uncaging of compounds, and femtosecond laser microsurgery. We show in **Figure 2-3a** an example of how the system can be used to study neuronal regeneration following injury by laser microsurgery. The lateral-neuron axon fiber bundle projecting along the trunk of a larva is visible when the larva is laterally oriented. We perform subcellular-precision laser axotomy by focusing near-infrared femtosecond laser pulses [2]. The surgery function is semi-automated to achieve high throughput: The user selects a cell body by clicking on a graphical user interface. An algorithm estimates the distance from the cell body to the point of axotomy along the axon. The position stage automatically moves the axonal region to be axotomized to the focal spot of the laser. The regenerating axonal fibers are shown at 18 and 24 hours post-axotomy in **Figure 2-3a**. The laser pulses were delivered with high precision (1.7 μm), and the subsequent response of the tissue to the laser (i.e. immediate retraction of nerve fibers) showed variability ($\pm 5.5 \mu\text{m}$) (**Figure 2-3b**).

Collateral damage was insignificant: 100% of the animals recovered from surgery within 30 minutes with no apparent morphological abnormality, and 100% of the animals survived 24 hours post surgery.

A complete cycle of loading, positioning, subcellular-resolution imaging, and dispensing an animal takes less than 16 seconds. The laser surgery operation requires an additional 2 seconds. Screening an entire multiwell plate took 31.85 minutes with an average $19.9 \text{ seconds}\cdot\text{well}^{-1}$, which includes the additional interval for retracting, moving and inserting the loading apparatus, and sealing the wells. Performed manually, assays of similar complexity require about 10 minutes per animal, and the error rate is much higher.

We have performed health assessment on $n = 450$ larvae screened at 2 dpf at three different initial aspiration rates (**Fig. 2-4a**). The health assessment was based on both functional and morphological criteria measured at $t = 0+$, 12, 16, 20, 24, 28, 32, and 36 hours. Functional criteria included visual confirmation of normal heartbeat and reflex response to touch stimuli. Morphological criteria included bending (i.e. lordosis, kyphosis, and scoliosis) and craniofacial abnormalities. At all flow rates, heartbeat and touch response matched those of controls. Tearing of yolk was never observed ($n = 450$). At the highest initial flow rate of $330 \mu\text{l}\cdot\text{s}^{-1}$, 2.0 % of the animals exhibited morphological abnormality. When the loading speed is slightly slower, all health criteria matched those of controls (**Fig. 2-4a**). Post manipulation developmental delay was measured by monitoring the time of appearance of the swimming bladder. There was no significant difference with

single-tailed t-test ($P = 0.94$) between the development of larvae that were manipulated by the system and control animals, even at the highest flow rates (**Fig. 2-4b**). Among the different larval age groups tested (i.e. 2-7 dpf, $n > 100$ per age), no statistically significant difference in health assessment was observed in comparison to the results for 2 dpf larvae (see **4-5 Health Assessment**).

2-3 Hardware/Software Architecture and Operation

Imaging and Laser Axotomy

The imaging system (**Fig. 2-1**) consists of a dual (upright/inverted) microscope (Eclipse Ti, Nikon (inverted), Nikon 90i Digital Imaging Head (upright)) with two light sources (Mercury lamp, Nikon). The upright microscope's top port is equipped with a multi-beam laser confocal scanning head (Infinity3, VisiTech) with a 1004 x 1002 pixel EMCCD camera (iXon+885, Andor Technology) for high-speed confocal imaging. For high-speed image sectioning, a piezo actuator with 400 μm travel distance (P-725 PIFOC, Physik Instrumente) holds either a 10x, 20X, or 40x water immersion lens (Nikon). A tunable femto-second laser (Mai Tai, Spectra-Physics Lasers) is guided to the upright microscope for laser axotomy. A high-speed CCD camera (GX-1050, Prosilica) is connected to the side port of the inverted microscope for larva detection, position and rotation.

Capillary stage

Two precision stepping motors (KP35FM2-044, Japan Servo Co.) hold a capillary along its axis of rotation as shown in Fig. 1. The motors are controlled by a microstepping driver (BSD-02LH, Interinar Electronics). The motor and capillary assembly is mounted on a 3-axis precision stage (MP-200, Sutter Instrument) with 0.04 μm resolution along each axis.

High-Speed photodetection

The photodetection system (**Fig. 2-1**) consists of a photodiode IC (OPT301, Texas Instruments) and two LEDs (Cree Inc) aligned in transmission and reflection configurations as shown. The photodiode IC contains an integrated amplifier.

Multiwell plate/ reservoir loading

The system can load larvae from reservoirs or multiwell plates (**Fig. 2-1**). The multiwell plate loading stage is comprised of 3 linear precision motors (RCA2, Intelligent Actuators). The motors are controlled by RACON 20/30 drivers (Intelligent Actuators). The loading head consists of two tubes (New England Small Tubing Inc.) inserted into a silicone rubber block. The silicon rubber block is pressed (by the loading stage motor) against the top of the multiwell plate to seal the wells. One tube aspirates the larva from the sealed well, while the other tube injects water.

Fluidic Pumps and Switches

Larvae are delivered to the capillary under the objective lens through a syringe pump (Carvo XLP6000, Tecan Systems). Two fluidic valves (075P2NC12, Bio-Chem Fluidics) are used to switch the flow between the reservoirs and multiwell plate by pinching the silicone tubing (1/32" ID x 3/32" OD, Bio-Chem Fluidics).

Computer Interface and Control

Two NiDAQ input/output data cards (PCI-6512 and PCI-6259, National Instrument) are mounted in a DELL OptiPlex computer to control the fluidic valves, stepping motors, and reading out the voltage across the photodetector. The control software is written in Matlab.

Algorithm for Operation Sequence

The detailed algorithm for operation sequence of the system is shown in the flowchart of **Figure 2-5**. The rectangles, parallelogram, and rhomboids represent the actions, measurements, and conditionals, respectively.

The system starts by initializing syringe pumps, cameras, lamps, shutters, position stages, and motors. The fluidic valves (**Fig. 2-1**) are switched to the source of fish i.e. either multiwell plate or fish reservoir. The larva is aspirated from the selected source at a constant rate of acceleration of $42 \mu\text{l/s}^2$ up to a maximum speed of $330 \mu\text{l/s}$. The photodetector is continuously sampled at 2 kHz rate via the NiDAQ PCI-6259 card until the intensity reading crosses a pre-determined threshold (the value of threshold is calibrated in advance by trial and error). Upon detection of

the larva the fluidic valve is switched to the water reservoir if the larva is being loaded from the fish reservoir. The aspiration rate is subsequently decreased to 83 $\mu\text{l/s}$ to avoid damaging the larva at the entrance of the capillary. The high-speed CCD at the bottom port is continuously reading at 100 frames/second. The pixel intensity is averaged over the entire field-of-view, and compared to a pre-determined threshold (Value of threshold is calibrated in advance by trial and error). When average pixel intensity drops below the threshold, the aspiration is stopped.

The capillary is then rotated via the motors until the larva is at the desired orientation. A large field-of-view image of the gross morphology of the larva is acquired and stored by the CCD at the bottom port. The motorized shutter of the inverted microscope (i.e. bottom shutters) is closed while that of upright microscope (top shutters) is opened. The image acquisition is switched from the bottom CCD to either the top CCD or the high-speed scanning confocal head equipped with EMCCD. Guided by fluorescence imaging, the region of interest is located. Either confocal stacks or wide-field fluorescence images are acquired. The top shutter is closed, and the bottom shutter opened. The image acquisition is switched to the bottom port. The system is now ready for the next cycle of operation.

Figures

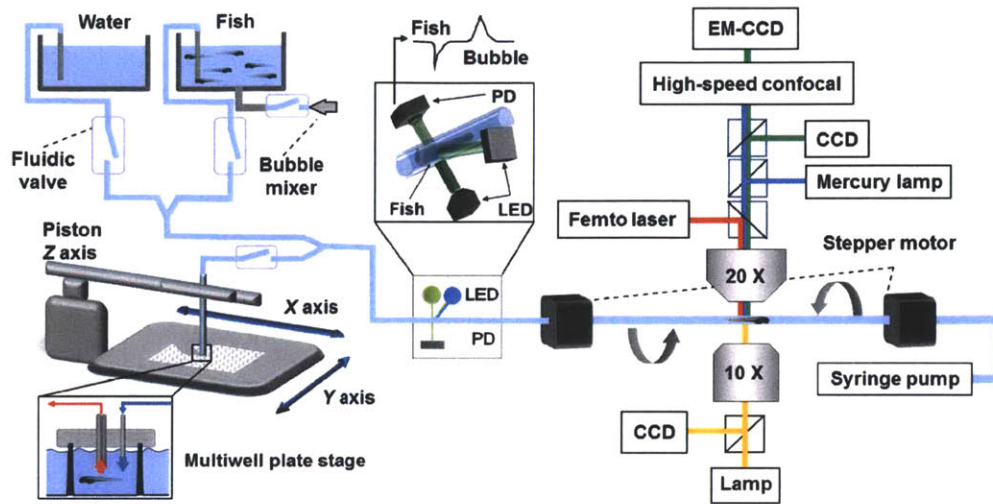


Figure 2-1. Zebrafish manipulation and imaging platform. Larvae are automatically loaded to the system from either reservoirs or a multi-well plates. Reservoirs of larvae and water are connected to the system via fluidic valves. A bubble mixer prevents settling of the larvae to the bottom of the reservoir. The multiwell plate sits on a motorized x-y stage, which positions individual wells below a larva-loading and a water-supply tube (diameters 1.0 and 0.2 mm, respectively), both held by a silicone rubber block. The silicon rubber block seals the well surfaces as a piston moves the loading and supply tubes into the wells. A photodetection system including two LEDs and one high-speed photodiode in transmission and reflection configurations discriminates the passage of a larva from air bubbles and debris with 100% reliability ($n = 1000$). Two stepping motors hold a capillary of diameter $800\ \mu\text{m}$ along its axis of rotation. The motor and capillary assembly is mounted on a 3-axis position stage (not shown) and held below an upright either

10x (NA = 0.5) or 20x (NA = 1.0) or 40x (NA = 0.8) water-immersion objective lens for confocal imaging and an inverted 10x air objective lens for bright-field imaging. A multifocal confocal head with a cooled electron-multiplying (EM) CCD camera is connected to the microscope's upright port for high-speed confocal fluorescence imaging. A second upright cooled camera with large-area CCD allows wide-field fluorescence imaging. A high-speed CCD camera connected to the inverted port allows rapid bright-field detection and positioning of larvae. A femtosecond laser beam used for microsurgery is directed to the upper beam path by a dichroic filter and focused on the sample through the objective.

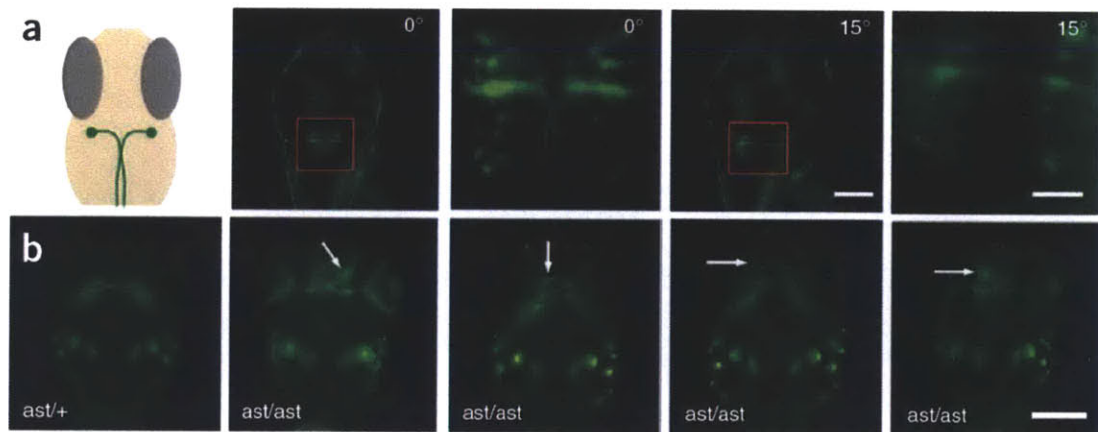


Figure 2-2. Orientation, imaging, and screening of zebrafish larvae. **(a)** Schematic of Mauthner cell neuroanatomy on the left showing the midline crossing of Mauthner axons. Confocal images of EGFP expressing Mauthner cells at 0°, 15°, and 45°. The midline crossing of Mauthner axons in the hindbrain is visible only in the 0° view. Scale bar 150 μm (50 μm for insets). **(b)** An illustrative genetic screen.

GFP labeled axons of retinal ganglion neurons projecting to the optic tectum fail to exhibit proper midline crossing in homozygous astray ($ast^{+/+}$) zebrafish, while the projections are normal in heterozygous ($ast^{+/-}$) zebrafish. Genotypically homozygous $ast^{-/-}$ and $ast^{+/+}$ fish were crossed to generate $ast^{+/-}$ larvae. A 96-well plate was randomly and partially populated with the heterozygous $ast^{+/-}$ progeny. The rest of the wells were populated with the homozygous progeny of $ast^{+/+}$ fish. A blind screen was performed by loading the animals from multi-well plates and orienting them to visualize midline crossing as in part (a) by a 10x (NA = 0.5) objective lens with long depth-of-focus in wide-field fluorescence imaging mode. Animals were blindly classified according to the observed phenotype. White arrows in the representative images of the range of phenotypes screened point to the misguided projections that led to the indicated phenotypic classifications. True positive rates of 100% and 98.80% were achieved for identification of $ast^{+/-}$ and $ast^{+/+}$ animals, respectively. The 1.20% false negative error in identification of $ast^{+/+}$ animals was due to the rare cases of mutants with strong phenotypic similarity to wild type. Scale bar 150 μm .

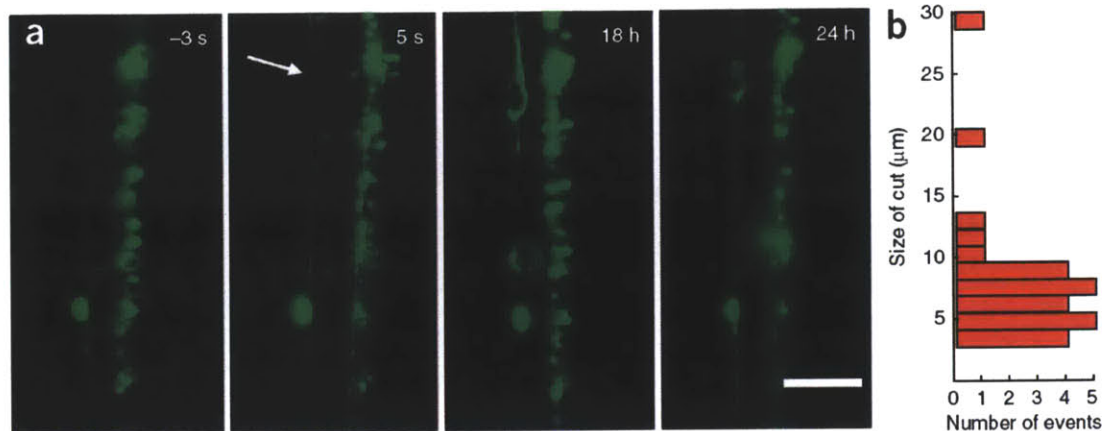


Figure 2-3. Subcellular femtosecond laser microsurgery and subsequent neuronal regeneration. **(a)** Femtosecond laser micro-axotomy of lateral-neuron axon fibers in a 3 dpf larva laterally oriented by the system. Wide-field fluorescence images are shown at 3 sec pre-axotomy, and 5 sec, 18 hours, and 24 hours post-axotomy respectively. The axon fiber is cut 850 μm distance from the soma using ultrashort laser pulses with 780 nm wavelength, 100 fs duration, 12.7 nJ pulse energy, 80 MHz repetition rate, and 10 ms long pulse train focused by a 20x NA = 1.0 objective lens. **(b)** Statistics of laser cut sizes were quantified with 40x NA = 0.8 objective lens. Surgeries were repeated on $n = 30$ animals with 100% success rate. The laser was focused with a precision higher than 1.7 μm . The results were measured 5 seconds after surgery and cuts had an average size of $8.1 \pm 5.5 \mu\text{m}$. Scale bar 75 μm .

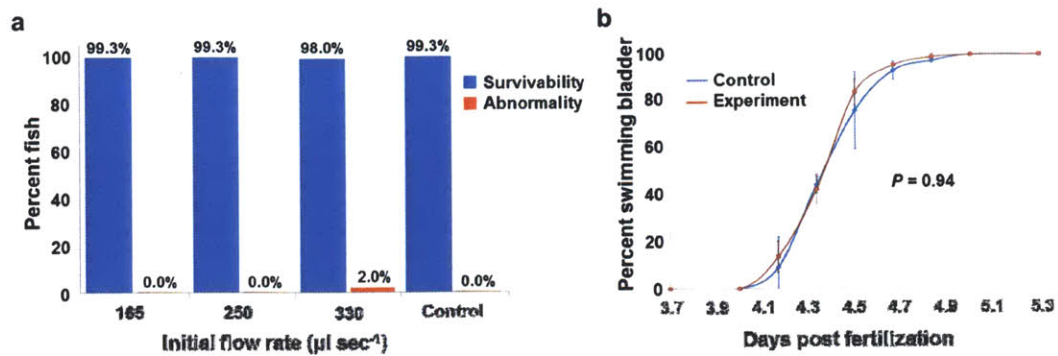


Figure 2-4. Quantitative assessment of throughput and animal health. (a) Assessment of animal health. The syringe was operated at three different initial aspiration rates of 165, 250, and 330 $\mu\text{l}\cdot\text{s}^{-1}$ for loading 2 dpf larvae from multiwells. $n = 450$ larvae in total were anesthetized with 0.20 mg·ml⁻¹ Tricaine, loaded, and dispensed from the platform. A control group of $n = 150$ larvae from the same breed were similarly anesthetized. The survival rate (blue column) at the maximum initial flow rate of 330 $\mu\text{l}\cdot\text{s}^{-1}$ was 98.0%. The health assessment was based on both functional and morphological criteria measured at $t = 0+$, 12, 16, 20, 24, 28, 32, 36 hours: Functional criteria included visual confirmation of normal heartbeat, and reflex response to touch stimuli. Morphology criteria included bending (i.e. lordosis, kyphosis, and scoliosis) and craniofacial abnormalities. Our criteria included those injuries even if the animals regenerated later. At all flow rates shown in Fig. 5b, heartbeat and touch response matched those of controls, and tearing of yolk was never observed ($n = 450$). At the highest initial flow rate (330 $\mu\text{l}\cdot\text{s}^{-1}$), only 2.0% of the animals exhibited morphological abnormality. Furthermore, when the loading speed is slightly slower (increasing the screening

time approximately only by 1 second), all health criteria matched those of the controls. (b) The appearance time of swimming bladder showed no significant variation between experiments (blue line, n = 50) and controls (red line, n = 50), indicating no developmental delay. Experiment was repeated 3 times.

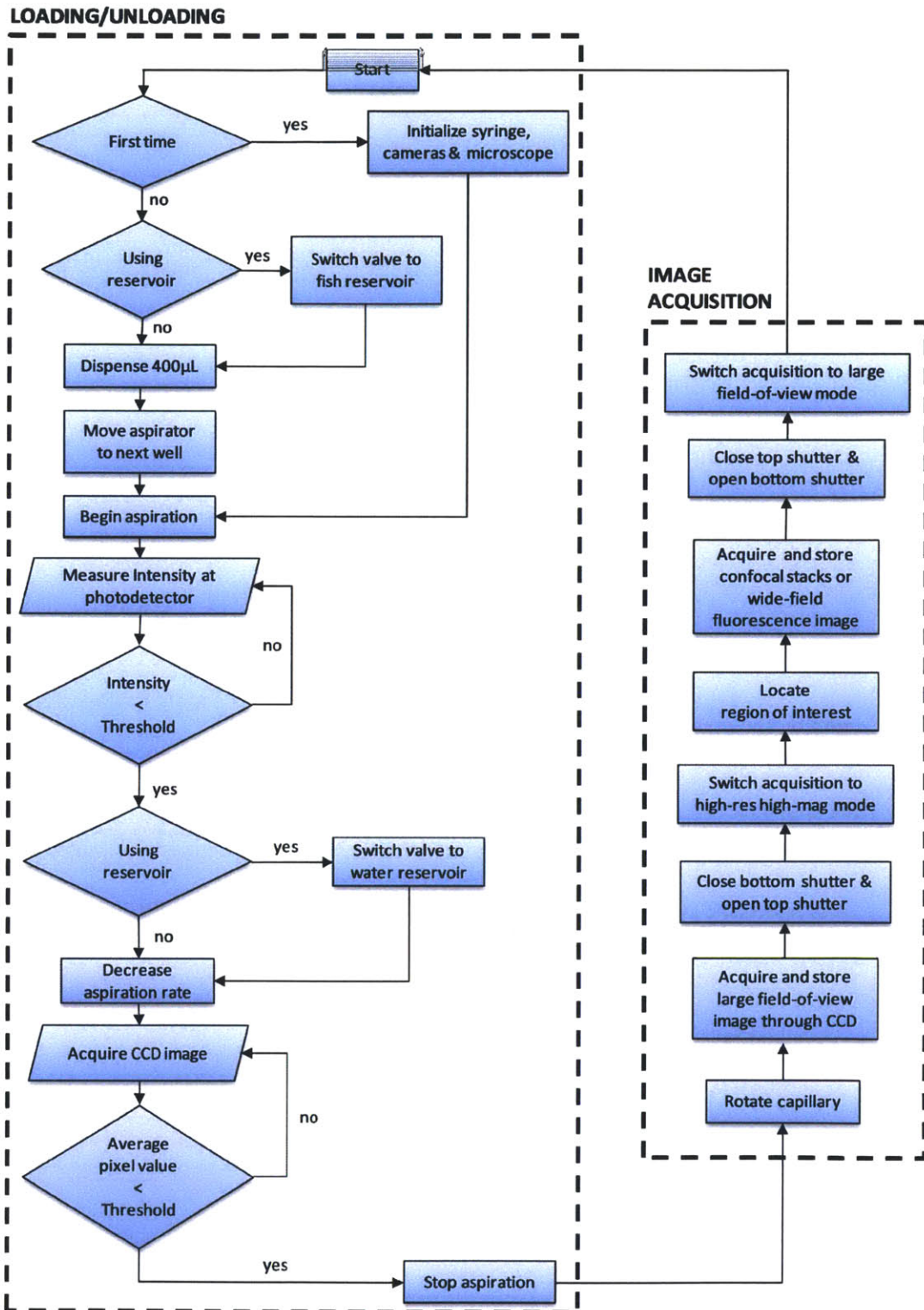


Figure 2-5. Flowchart showing the algorithm for the operation sequence of the system.

References

1. Chang, T.Y., et al., *Fully automated cellular-resolution vertebrate screening platform with parallel animal processing*. Lab Chip, 2012. **12**(4): p. 711-6.
2. Pardo-Martin, C., et al., *High-throughput in vivo vertebrate screening*. Nat Methods, 2010. **7**(8): p. 634-6.

Chapter 3

Pipelining of processes and optimization of VAST

3-1 System Setup

In order to improve timing and reliability of VAST system, we demonstrated the multi-thread VAST system loads larvae automatically from a 96-well nylon mesh plate that fits into a matching 96-well tray (MultiScreen-Mesh Plate, Millipore Inc.). The multiwell plate is brought into position by a three-axis motor stage (RCA2, Intelligent Actuators). The mesh-filter insert allows easy transfer of larvae. In order to keep the water level constant, two tubes separately aspirate and dispense water (**Figure 3-1 insert A**) via the syringe pump. Larvae are detected as they pass through the high-speed zebrafish discriminator, which distinguishes larvae from air bubbles and debris and also differentiates fluorescent from non-fluorescent larvae. The design of the zebrafish discriminator is discussed in detail below. Two high-precision step motors (KP35FM2-044, Japan Servo Co.) hold an ultra-thin glass capillary along its axis of rotation. The capillary has an outer diameter of 700 μm and a wall thickness of 10 μm (BGCT 0.7, Capillary Tube Supplies) and is immersed in a water bath to minimize the index of refraction mismatch. The assembly (i.e. motors, capillary and water bath) is mounted on a

three-axis position stage (MPC-200, Sutter Instrument) and held between an upright microscope for epi-fluorescence (and confocal) imaging and an inverted microscope for bright-field imaging. The inverted microscope is connected to a high-speed CCD (GX-1050, Prosilica) and is primarily used to detect, position, and rotate the larvae. A high-speed confocal head (Infinity 3, VisiTech Inc.) with a cooled EM-CCD (iXon+885, Andor Technology) is used for confocal imaging. The fluidic elements are controlled by three pinch valves (075P2NC12, Bio-Chem Fluidics) and three computerized syringe pumps (XLP 6000, Tecan). Fluidic components are connected through silicone tubing (0.8 mm inner diameter, Bio-Chem Fluidics). The entire system is controlled via a code written in MATLAB.

3-2 Multi-thread Operation

The multi-thread VAST system simultaneously performs three independent operations to enable parallel processing of multiple fish; loading, imaging, and unloading. At the beginning of each cycle, a larva is acquired from a multiwell plate by syringe pump 1 and the zebrafish discriminator is activated to distinguish the contents of the flow (i.e. larvae versus debris or bubbles). After the discriminator detects a larva, pinch valve 1 is opened and syringe pump 1 is stopped, allowing the larva to transit from the loading module to the imaging module. The larva is transported into the imaging module via syringe pump 2 after the flow direction is changed by switching pinch valves 2 and 3. The loading

module continuously repeats these steps and each loading cycle takes 4 seconds to complete. In the imaging module, the larva is automatically positioned, rotated, and imaged inside the capillary, which takes 9.6 seconds on average. The timing for imaging was calculated for a single wide-field fluorescence acquisition with a 300 ms exposure time. The larva is then moved to the unloading module and a new larva is transported into the capillary from the loading module. The larva in the unloading module, (held between valve 3 and the imaging module), is then transferred into its corresponding well of the output multiwell plate. Each unloading cycle takes 3.4 seconds and dispenses 500 μL of medium with a flow rate of 165 $\mu\text{L}/\text{sec}$. Timing analysis is based on trials of $n=192$ animals. As reported previously, over 98% of larvae imaged by VAST survive and develop without noticeable morphological abnormalities [1]. By multi-threading the loading, imaging and unloading operations, throughput becomes limited only by the slowest operation (i.e. the imaging step; 9.6 seconds), rather than by the total time required to carry out all processes (**Figure 3-2**).

3-3 Fluorescence/bright-field automated zebrafish discriminator

A low-cost, high-performance discriminator (**Figure 3-3a**) is used to distinguish larvae from debris and air bubbles and to separate fluorescent and non-fluorescent larvae. The discriminator is formed by a bright-field photodetection system and a fluorescence-activated larva sorter. The bright-field photodetection

system is comprised of an integrated photodiode and an amplifier chip (OPT301, Texas Instruments) and two LEDs aligned in transmission and refraction/scattering configurations. The fluorescence-activated sorter consists of an epi-fluorescence detection system with a GFP filter set, a 10X lens, a photo-multiplier tube (PMT), and a mercury light source. By simultaneously measuring transmitted light and refracted/scattered light at different wavelengths, this device can reliably discriminate between larvae, debris, and air bubbles based on the refraction/transmission ratio of different objects (**Figure 3-3b**). The transmitted light can largely pass through the fluidic tube when the tube is filled with solution. When an object or bubble crosses the light path, the light is absorbed/refracted/scattered and therefore the transmission light intensity received by the photodiode decreases. A live larva tends to absorb light more than scattering it, while a dead larva, debris, or bubble tend to scatter light more than transmit it. To balance the scattered and transmitted light intensity on the detector, we use two LEDs where one is in the transmission path and the other is in the orthogonal scattering path. LEDs with different emission colors are used to aid the alignment of the refraction/transmission ratio. Although the scattered light intensity is significantly lower, the intensity of the LEDs did not require any tuning because of the significant difference in the spectral responsivity of the photodiode to the LEDs' colors. Such discrimination of multicellular organisms has traditionally been performed with more complicated setups and image processing algorithms. The reliability of our discriminator was tested under a variety of flow rates,

ranging from 165 $\mu\text{L}/\text{sec}$ to 495 $\mu\text{L}/\text{sec}$ (**Figure 3-3c**). For the flow rates that we use in screening (330 $\mu\text{L}/\text{sec}$), the reliability is near 100 %.

3-4 Identification of zebrafish orientation and position

A key step in the design of VAST is the automation of the fine positioning of the region of interest (ROI) within the relatively small field-of-view (FOV) of the high power objective lenses used for cellular-resolution imaging. To accurately and consistently image the same ROI across many larvae, it is necessary to precisely control both position along the length of the capillary and orientation/rotation around the fixed axis of the capillary. Due to the phenotypic variations that can occur in large-scale genetic and chemical screens, a reliable and flexible algorithm is crucial.

Our algorithm works through a four-step process; coarse positioning of the larva under the FOV, calculation of the direction of its entry into the capillary, identification of its orientation and rotation, and fine positioning of the ROI within the FOV of the high power objective lens.

The coarse positioning of the larvae in the center of the FOV is done through a closed loop feedback between the CCD imaging the FOV and the computer-controlled syringe pump as previously described [1].

Larvae can enter the capillary in either a head- or tail-first orientation. For this reason, the longitudinal (head vs. tail) orientation of the larvae has to be identified before any image processing steps are performed. A 1D pixel intensity profile $f(x)$ for the fish can be computed by summing the pixel intensities across the axis orthogonal to the main tube axis. The center of mass (of pixel intensities), CM, of the larvae is computed by summing the position values weighted by the normalized 1D intensity profile.

$$CM = \frac{\sum_{x=1}^n f(x)x}{\sum_{x=1}^n f(x)}$$

The largest intensity variation between the zebrafish and surrounding water/tubing occurs at the very tip of the head, x_0 , which is identified by finding the position of maximum value of f' , the derivative of the 1D intensity profile. The center of mass falls in the upper part of the abdomen, and therefore the orientation of the larvae can be found by comparing the geometrical center to the center of mass of the fish.

$$D = \begin{cases} 1, & CM - x_0 > 0 \\ 0, & CM - x_0 = 0 \\ -1, & CM - x_0 < 0 \end{cases}$$

Where $D = 1$ ($D = -1$) means that the head is towards left (right).

We next identify the lateral orientation of the larva. Due to the anatomical symmetry and optical transparency of the larvae, it is unreliable to identify the lateral orientation based only on the ventral and dorsal views (Figure 3-4a). Instead, we acquire a series of 2D images of the larva $f(x,y)$ at a constant frame

rate of 180 frames per second (fps) while rotating the capillary 360 degrees at a constant rotation speed at 2 sec/cycle (Figure 3-4b). Using the frame acquisition rate and rotation speed, a rotation angle is assigned for each acquired frame. We then compute the cross correlation [2], CC, between each frame and predefined template intensity distributions $t(x, y)$ of age-matched larvae imaged at dorsal and lateral views using the following relationship:

$$CC(f, t) = \max_{u,v} \left(\frac{\sum_{x,y} [f(x, y) - \bar{f}_{u,v}] [t(x - u, y - v) - \bar{t}_{u,v}]}{\left(\sum_{x,y} [f(x, y) - \bar{f}_{u,v}]^2 \sum_{x,y} [t(x - u, y - v) - \bar{t}_{u,v}]^2 \right)^{\frac{1}{2}}} \right)$$

Where $\bar{f}_{u,v}$ and $\bar{t}_{u,v}$ are the average pixel values for the image and template, respectively. The cross-correlation with the dorsal template yields two narrow peaks at the dorsal and ventral orientations (Figure 3-4c). However, these peaks alone are insufficient to distinguish between dorsal and ventral sides. The cross-correlation with the lateral template yields a single wider peak that identifies the right versus left side of the fish. This knowledge of left/right orientation and the direction of rotation are then used to differentiate which peaks from the dorsal template corresponds to the ventral vs. dorsal orientations. To handle phenotypic variation across larvae, we have constructed a collection of templates for larvae under the typical morphological abnormalities (e.g. pericardial edema). When the maximum cross correlation between the templates and the larva does not exceed a user defined minimum, our algorithm looks through this collection of templates and recalculates the orientation using the template with the highest correlation. If

the cross correlation does not reach a user-defined threshold for any template, the larva is discarded. The reliability of the orientation algorithm is 99 % (n=100 larvae).

Once the dorsal, ventral, and lateral orientations have been identified, the larva is automatically rotated for imaging at the predefined angle specified by the user (e.g. dorsally to image the brain, ventrally to image the heart and brachial arches, obliquely to image the pancreas). At this orientation, the ROI is defined by matching the larva to a third template of aged-matched larvae at the desired angle which contains the location of the ROI.

3-5 Analysis of capillary materials for high- quality imaging

Confocal imaging necessitates both low autofluorescence and low optical aberrations. Since larvae are imaged through a capillary in VAST, the choice of capillary material is a critical factor in achieving distortion-free, low-background, high-resolution imaging. A previous study [3] reported that Teflon tubes offer optimal quality for bright-field imaging of larvae within capillaries, due to the matched refractive index with water. However, limited quantitative data has been reported for fluorescence imaging, which is crucial for most experiments. Polymers such as PTFE (polytetrafluoroethylene) and FEP (fluorinated ethylene propylene), two types of Teflon, cause significant autofluorescence. This

dramatically decreases the signal-to-noise ratio (SNR) and lowers the quality of fluorescent images. On the other hand, glass capillaries with ultra-low autofluorescence and extinction coefficients are not refractive index-matched to the surrounding water, which can create distortions and lead to decreased confocality and axial resolutions.

We have tested four capillaries of different materials and thicknesses and quantitatively evaluated the point-spread functions (PSF) of the resultant confocal images. GFP-tagged fluorescent micro beads (0.2 μm in diameter) were mixed in 2 % Type IV optical agarose (Sigma, A3643) to avoid Brownian motion. The beads were then imaged with a multifocal confocal system with pinhole size of 30 μm , through a 100x 1.1 NA water dipping objective (Nikon Instruments). The beads trapped within the agar mold (index matched to water) were imaged either without any intervening glass, inside a PTFE capillary with a wall thickness of 250 μm (Zeus Inc.), inside an FEP capillary with a wall thickness of 150 μm (Zeus Inc.), inside a borosilicate capillary with a wall thickness of 170 μm (Wale Apparatus Co.), or within an ultrathin borosilicate capillary tube with a wall thickness of 10 μm (Capillary Tube Supplies Ltd.). Figure 3-5a shows a cross-section in the radial and axial planes through the center of a bead for each of the conditions.

We computed the axial full-width half-maximum (FWHM) of the PSFs without a capillary and when using the FEP, 170 μm thick borosilicate, and the 10 μm thick borosilicate capillaries. The FWHMs were 1.2 μm , 1.4 μm , 2.6 μm and 1.1 μm , respectively (Figure 3-5b). Due to the optical aberrations that cause non-Gaussian

like PSFs on the PTFE capillary, we were unable to compute a FWHM. Importantly, our analysis shows that the 10 μm thick borosilicate capillary produces significantly less image distortion than the Teflon capillaries with refractive indexes closer to water. Furthermore, our autofluorescence analysis demonstrates that, unlike borosilicate, both types of Teflon (i.e. PTFE and FEP) cause significant autofluorescence (Figure 3-5c). Thus, we conclude the ultrathin (10 μm thick) borosilicate capillary is the most appropriate choice for high-resolution confocal imaging.

3-6 Conclusions

Here, we have demonstrated a fully automated multi-threaded vertebrate screening platform. To significantly increase throughput, we modularized the system into three independent sections that can process multiple zebrafish in parallel. In this configuration, system throughput is limited only by the image acquisition speed rather than by the speeds of fluidic and mechanical processes. A discriminator differentiates the entry of a fluorescent larva from non-fluorescent larva, air bubbles, and small debris. A simple and highly reliable algorithm is implemented for automated identification of the position and rotational angle of the larva. Furthermore, to identify the best capillary materials for confocal and fluorescence imaging, we analyzed various capillaries measuring their PSFs and autofluorescence. We showed that ultra-thin borosilicate capillaries (with wall

thickness of 10 μm) provide the highest-resolution distortion-free low-background images.

3-7 Algorithm and Software for Operation Sequence

The detailed algorithm for the operation sequence of the system is shown in the flowchart of the *Figure 3-6*. The control software is written in Matlab.

Figures

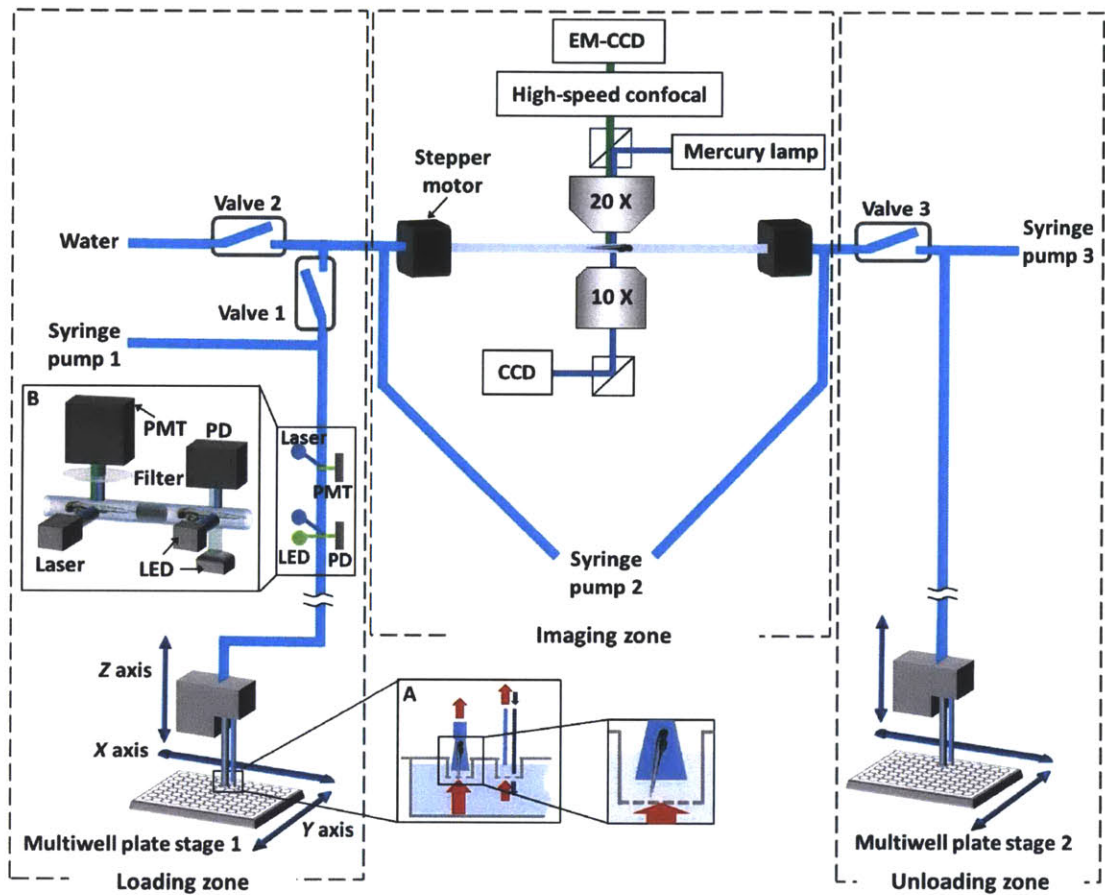


Figure 3-1 Multi-thread Vertebrate Automated Screening Technology (VAST). The platform consists of three subsystems that operate simultaneously: loading, imaging, and unloading. Larvae are automatically loaded to the platform from individual wells of a mesh-filter multiwell plate positioned by a motorized x-y stage. The mesh-filter insert allows easy transfer of larvae into the system. In order to maintain the water level, a circulation device is set nearby the loading nozzle (inset A). A zebrafish discriminator with a brightfield and a fluorescence photodetection system (inset B) discriminates the passage of fluorescent larvae

from non-fluorescent ones, air bubbles and debris. Two step motors hold a capillary immersed in a water bath along its axis of rotation; this assembly is mounted on a three-axis position stage (not shown) and held between an upright microscope and an inverted microscope. A multifocal confocal head with a cooled electron-multiplying charge-coupled device (EM-CCD) camera and a second large-area charge-coupled device (CCD) are used for high-speed confocal and wide-field fluorescence imaging, respectively. A high-speed CCD camera connected to the inverted microscope allows rapid bright-field imaging for positioning and orienting the larvae.

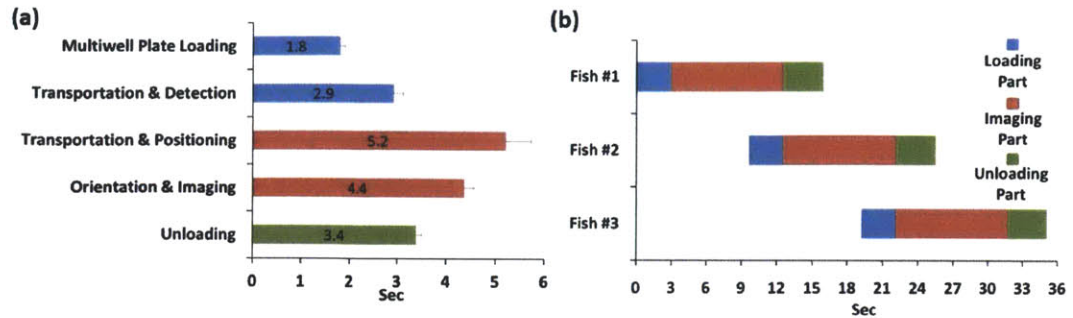


Figure 3-2 Timings of multi-thread processing of zebrafish. Blue, red, and green bars indicate the processes comprising loading, imaging, and unloading, respectively. (a) The time required for each handling step (n = 192). (b) Multi-thread operation: The system simultaneously performs loading, imaging, and unloading operations with three different larvae. As a result, the overall processing time is dictated solely by the duration of the slowest process (i.e. positioning + imaging; 9.6 sec), not by the total duration of all processes.

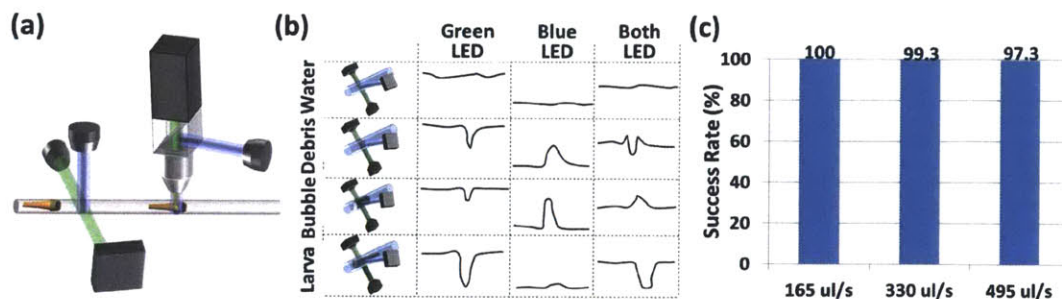


Figure 3-3 Zebrafish discriminator. (a) Schematic representation of the zebrafish discriminator. The system is composed of a bright-field discrimination system and a fluorescence-activated zebrafish sorter. (b) Schematic representation of the

mechanism of action of the bright-field discrimination system. By combining both the refracted/scattered and transmitted signals the system distinguishes a zebrafish larva from air bubbles and debris. (c) Detection and discrimination reliabilities at increasing flow rates. The reliability is near 100 % at normal operating speeds of 330 $\mu\text{L/s}$. (n=150).

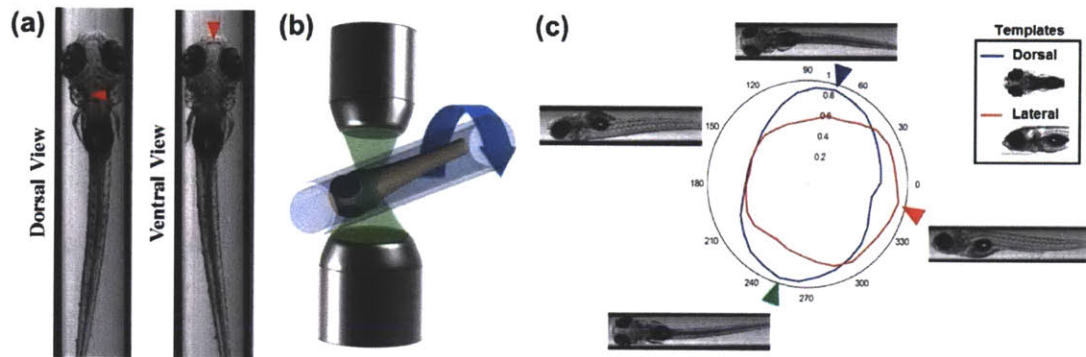


Figure 3-4 Identification of the angle and position of larvae. (a) Dorsally and ventrally oriented larvae. Red arrows indicate the dominant morphological features for distinguishing dorsally vs. ventrally views. It is too difficult to reliably determine the larva's orientation based solely on comparisons with dorsal and ventral reference images. (b) The larva is rotated along its longitudinal axis through a full 360° and snapshots are acquired at two degree increments at 180 frames per second. (c) The system then correlates the images with a library of prerecorded dorsal and lateral images from stage-matched control larvae (inset). The blue and red curves in the radar chart are results of the image correlations with the dorsal and lateral templates. The blue, green, and red arrows indicate the

orientations of maximum correlations with the dorsally, ventrally and laterally orientated templates, respectively. The reliability of the algorithm is 99 % (n=100 larvae)

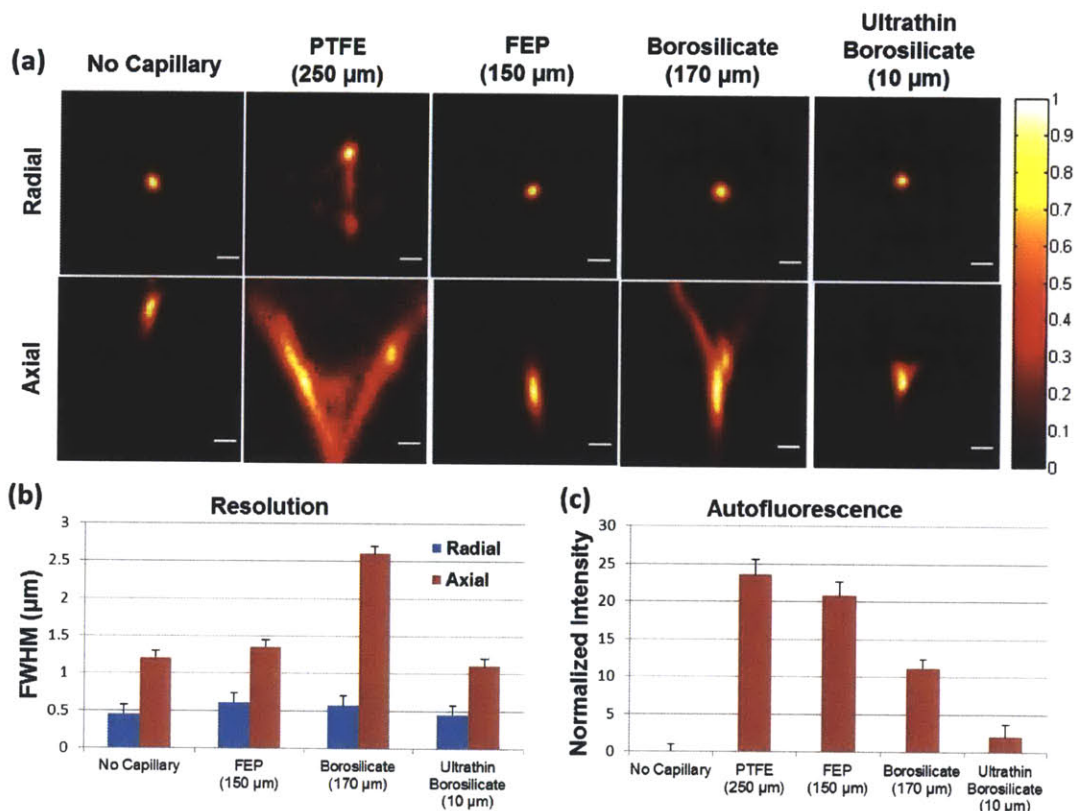


Figure 3-5 Analysis of capillary materials for distortion-free low-background high-resolution imaging. (a) From left to right, the point-spread functions (PSF) with different materials/conditions; no capillary, PTFE capillary, FEP capillary, borosilicate glass capillary, and ultra-thin borosilicate glass capillary. The wall thicknesses of capillaries are 250 μm , 150 μm , 170 μm and 10 μm , respectively (shown in brackets). The ultra-thin glass capillary produces the least image

distortion. Scale bar is 1 μm . (b) Radial (blue) and axial (red) resolutions of candidate materials. PTFE was not included due to the significant non-Gaussian PSF it produces. (c) Autofluorescence analysis of candidate materials. PTFE and FEP capillaries cause significant autofluorescence.

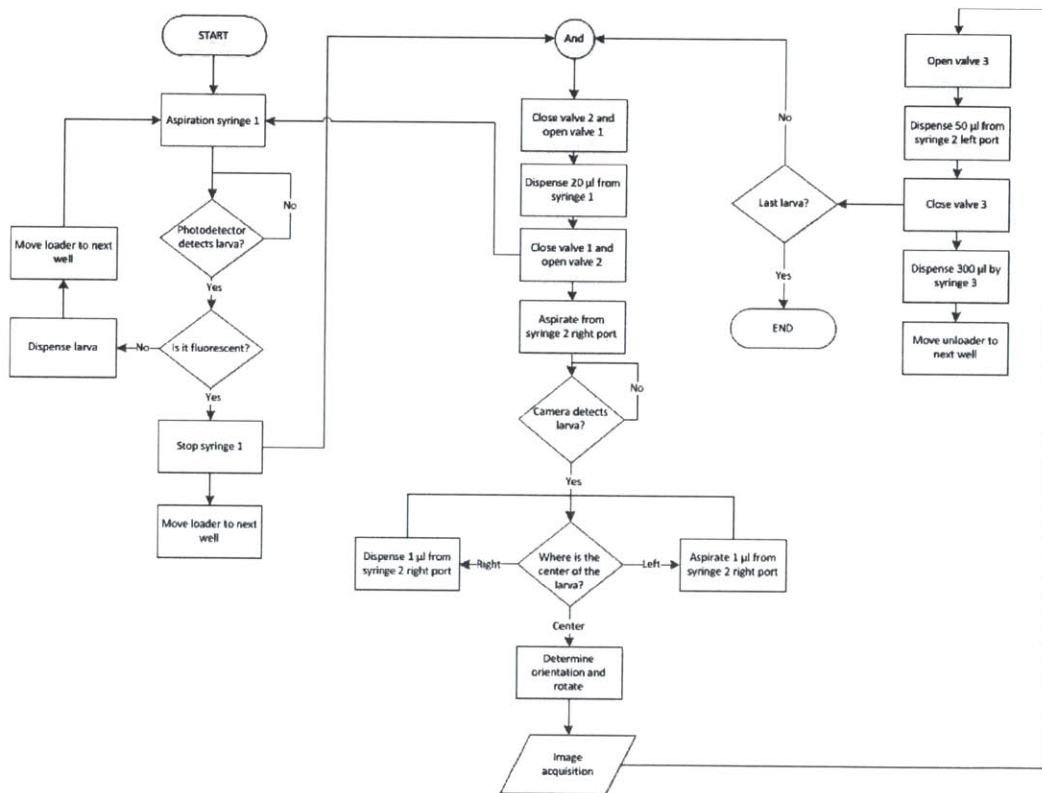


Figure 3-6 Flowchart showing the algorithm for the operation sequence of the system. Rounded rectangles show the initialization and endpoints of the flow chart. Square boxes show processing steps. Rhombus show conditionals or decision processes. Parallelograms show outputs (image acquisition). Circles represent waiting points, where both inputs have to be reached before proceeding to the

next step. The left section of the flow chart represent the loading subprocesses, the middle section the positioning and imaging subprocesses and the right section shows the unloading subprocess.

References

1. Pardo-Martin, C., et al., *High-throughput in vivo vertebrate screening*. Nat Methods, 2010. **7**(8): p. 634-6.
2. Briechle, K. and U.D. Hanebeck, *Template matching using fast normalized cross correlation*. Optical Pattern Recognition Xii, 2001. **4387**: p. 95-102.
3. Petzold, A.M., et al., *SCORE Imaging: Specimen in a Corrected Optical Rotational Enclosure*. Zebrafish, 2010. **7**(2): p. 149-154.

Chapter 4

Vertebrate Automated Microinjection Platform (VAMP)

4-1 Introduction

Biologics such as nucleic acids [1-3], proteins, cells [4], and nanoparticles [5] are under active investigation for the treatment of a wide variety of human diseases. In contrast to chemically synthesized small molecules, which have precisely defined structures and are typically engineered with enhanced solubility and permeability [6], biologics generally have structures that are generally much larger and far more complex, and therefore require sophisticated modes of delivery. Consequently, although large libraries of these materials are currently available [7-10], it remains challenging to rapidly assess their *in vivo* properties, such tissue specificity, pharmacokinetics, toxicity, and efficacy, in biologically relevant vertebrate models.

Zebrafish (*Danio rerio*) are increasingly used for chemical and genetic studies, and have the potential to become a powerful pre-clinical model for *in vivo* testing biological therapeutics. A unique combination of features, including small size, optical transparency, and rapid development, make zebrafish an advantageous vertebrate model for high-throughput screening

(HTS) [11, 12], which is cost-prohibitive in mammals, and lead to detection of adverse toxicity and off-target side effects in the early stages of pharmaceutical development [13, 14]. HTS of small molecules in zebrafish has identified novel biologically active compounds currently undergoing clinical trials [15]. Large-scale screening of biologics in zebrafish would offer similar advantages but is currently limited due to the absence of key technology for delivery of these materials to targeted organ or tissue of zebrafish. Usually, such delivery is done by manual microinjection [13], a process that is too slow and labor-intensive for HTS. Although automated microinjection systems have been developed for delivering nucleic acids and other agents into the yolk of pregastrula stage zebrafish embryos [14, 16], there are no existing high-throughput microinjection methodologies which can be readily applied to older embryos and larvae for precise targeting of specific organs and tissues.

Here, we demonstrate a vertebrate automated microinjection platform (VAMP for high-throughput injection and screening of biologic delivery vehicles in zebrafish larvae. We validated the functionality of VAMP by screening a library of structurally diverse amino-alkyl-acrylate and -acrylamide materials (to facilitate mRNA delivery), from which several formulations were identified to facilitate the delivery and local translation of protein-encoding mRNA in the central nervous system (CNS) of zebrafish larvae. These screening results were subsequently shown to be conserved in vivo in rodents, further validating the utility of the VAMP technology, which enables a dramatic increase in the throughput and complexity with which in

vivo assays can be performed. Deployment of VAMP into the screening field impacts a broad spectrum of both fundamental and translational research.

4-2 System Setup

The vertebrate automated microinjection platform (VAMP) consists of three major components: microfluidic larva handling, gel-droplet based larva arraying, and automated microinjection. One screening cycle includes five consecutive operations to a larva: loading, arraying, orientation/immobilization, microinjection of testing materials, and recovery of larvae from gel-droplet arrays (**Fig. 4-1**). Initially, larvae are kept in E3 media supplemented with 1% ultralow melting point (LMP) agarose, which remains liquid phase at room temperature (25 °C) and solidifies at 4 °C. Larvae are extracted from a 96-well plate with a mesh-filter insert, allowing easy transfer of larvae into the system [17]. A Light-Emitting Diode/Photodetector pair monitors the fluid path to discern the entry of larvae into the loading tube [18]. After loading and photodetection, a syringe pump dispenses each larva onto a flat pre-treated plate in an array format of single larva containing gel-droplets. The volume of each droplet is optimized according to array format: 25 µl for 96-spot array and 70 µl 24-spot array. To prevent mixing between each gel-droplet before solidifying, and also to ensure low contacting angle for easy imaging, the flat polystyrene plate are plasma treated with protection of a silicone mask to render 96 or 24 hydrophilic circular regions over a hydrophobic background, so that the dispensed gel droplets are isolated and

confined within the 96 or 24 hydrophilic spots. After arraying, the plate with arrays of single larva containing gel-droplets is transferred onto a temperature controlled stage with pulse vibrations. To access different organs of zebrafish, the larvae are placed into two basic orientations. For injecting into dorsal targets, larvae are agitated with pulses of vibrations, which induces startle response causing them to assume a dorsal-up orientation(**Fig. 4-2a-c**). For injecting into lateral and ventral targets, larvae are anesthetized by addition of 0.2 mg ml⁻¹ tricaine to the 1% LMP agarose, which causes the larvae to orient laterally (**Fig. 4-2d-f**). The dorsal and lateral orientation success rates based on agitating and anesthesia mechanisms for larvae of 4 day post fertilization (d.p.f.) are $93.4 \pm 6.6\%$ and $84.4 \pm 2.9\%$ (**Table 4-1**, n = 323). With the application of orientation mechanisms, we demonstrated successful microinjection of FITC-labeled dextran into different tissues or organs of larvae, including fore-brain (**Fig. 4-2b**), ventricle (**Fig. 4-2c**), eyes (**Fig. 4-2d**), heart (**Fig. 4-2e**) and liver (**Fig. 4-2f**) [19]

After proper orientation, single larva containing gel-droplets are solidified by cooling at 4 degrees °C with the temperature control module. Larvae are therefore immobilized within each gel-droplet. Then, the plate with larva droplets is transferred onto the automated microinjection platform consisting of a microinjection module, a long working distance objective with motorized Z-focus, an XY-axis stage, and a high-speed camera (**Fig. 4-1**). Using an in-house developed image recognition software (see **Section 4-4**), the system automatically locates each larva within a gel-droplet, positions and

zooms in the target region (brain ventricle) at the center of field of view. The injection micropipette is then lowered to approach the target tissue/organ gradually. The actual penetration of the micropipette tip into the larva is also determined by the software, which subsequently trigger the injecting operation. The overall success rate of the automated microinjection is 97.3% (n = 150), and the average deviation of injection site from the center of ventricle is $50 \pm 26 \mu\text{m}$ (distance, s.d., n = 75 from 3 separate experiments). After microinjection, a self-adhesive bottomless silicone multiwell chamber is attached to create 96 isolated wells containing the gel-droplets. Each well is then filled with E3 medium and the larvae are recovered and released by gentle flushing. It takes 20.0 ± 0.9 seconds to finish a complete cycle of loading, arraying, orientation, immobilization, automated microinjection and recovery of each larva, while the processing time can be further improved to 13.1 ± 0.5 seconds per larva with parallel processing (**Table 4-2**), which is achieved by independently perform larvae-arraying and microinjection. This is a significant improvement in the efficiency for handling zebrafish larvae, assays of similar complexity require about 5 min per larva, and the assays are error-prone [13]

To evaluate the ability to not affect the health of organisms in VAMP, we assessed the health of 478 larvae (4 d.p.f.) after running them through the system, including loading, arraying, orientation, immobilization, microinjection and recovery. The assessment was based on both functional and morphological criteria (see **Section 4-5**). For both survivability and

abnormality tests, operations by the VAMP show no significant evidence of adverse effect to the zebrafish larvae health, when comparing experimental set to control animal set. Notably, the few abnormal larvae in the experimental set gradually recover in the following few days after operations, and no obvious difference can be detected between the experimental and control animals 4 days after operations (**Fig. 4-3**).

4-3 Image Processing and Recognition

Initialization and autofocusing algorithm

For every microinjection cycle, the motorized microscope focuses on the microinjection tip which points the center of the view. Autofocusing process follows the initialization step (**Fig. 4-4a-c**).

For achieving automated microinjection, the first step is autofocusing. When we compare a focused and a defocused image, the difference between the two images is situated in the energy content on the higher frequencies in the spatial domain. Several experiments reveal that a simple high-pass filter for the spatial domain is sufficient for the desired implementation. The used algorithm is based on following convolution mask, resulting in the described high-pass characteristic. The spacing for this high-pass filter is 19.2 μm . (CCD pixel: 8 μm , optics: 0.6X, objective: 2X, Zoom: 2X)

$$k = \begin{bmatrix} 0 & -1 & 0 \\ -1 & 4 & -1 \\ 0 & -1 & 0 \end{bmatrix}$$

In order to find the focal plane, scanning through convoluted image value is very straightforward. In the VAMP system, the position of droplet holding plate is known and fixed. Therefore the maximum scanning range of the motorized microscope is not more than 400 μm , and the maximum step number is less than 10. In VAMP, the autofocus process is only needed to be executed during the starting point of the system and the process can be limited in 3 seconds.

Head/target recognition algorithm

The head or organs of larva is determined using a threshold-based algorithm which takes advantages of the recognition of the zebrafish eyes, yolk and the axis the fish body (**Fig. 4-4d**). In this algorithm, a threshold is set to find darkest parts of a larva: eyes and the yolk. After that, the axis of a larva is measured via rotated image-correlation with a saved template. Then, the profile of a larva can be determined by the line of centroids of eyes and the axis. The position of ventricle can be further located via shifting from the intersection of two lines. The optimal threshold value was determined via the optimization from distribution histogram. There were many factors that affect the threshold value and hence the algorithm accuracy, including the intensity of background light, the use of 1-phenyl 2-thiourea (PTU), the day of larvae and optical apparatus etc. The major factors were the stability of the light intensity generated from the power source, the orientation of the zebrafish larvae, and the agarose droplet size. For the injection process, it was observed

that, being oriented with a fixed-frequency vibration motor, all larvae tended to stay at the same vertical location.

Automated injection

Consequently, the injection process could be performed rapidly using the predetermined and fixed needle trajectory. Microinjection is the last step in an automated microinjection cycle (**Fig. 4-4f**). Two methods are using in this step. One, based on an ideal controlled condition, the distance between injection needle tip and the ventricle of a larva is known. And therefore, microinjection can be done by directly moving a specific distance of the needle. Another method involves monitoring the image change during the needle pressing on the head of larva. During the needle-pressing period, the deformation of tissue would increase the difference between the current and original images. However, after the needle penetrates tissues, the image difference will decrease rapidly. Our algorithm identifies the penetration process by detecting the decrease of image difference. In addition to the automated microinjection system, the semi-automated system, which allows full control of the needle via computer keyboard, was implemented in Matlab. Such semi-automated system was used as a complement to the fully automated system when different injection sites and extremely high injection precision are desired.

The results represented in **Table 4-3** were obtained from the agar-immobilized zebrafish larvae between 3 and 5 day post fertilization. In this

experiment, the depository destination was the zebrafish brain. For the determination of horizontal injection position, the injection site deviation was found to be $50.1 \pm 26.4 \mu\text{m}$ and it took 1.0 ± 0.1 seconds with the success rate of 96%. It was observed that if the algorithm that determined injection location was repeatedly run multiple times, the accuracy became better with a tradeoff of longer run time. For the injection process, it took 5.0 ± 0.1 seconds with the success rate of 97.33%.

4-4 System Hardware Architecture

The system starts by initializing syringe pumps (TECAN), a high-speed camera, lamps, shutters, position stages (IAI), a manipulator (Eppendorf), an injector (Sutter), Prior stage, and motors (Nikon). The fluidic valves (**Fig. 4-1**) are switched to the direction of flow. The larva is aspirated from the selected 96-well plate with mesh-insert at a constant rate of acceleration of $42 \mu\text{l/s}^2$ up to a maximum speed of $330 \mu\text{l/s}$. This 96-well plate is mounted with a temperature control module for maintaining liquid condition of LMP agarose solution. The photodetector is continuously sampled at 2 kHz rate via the NiDAQ PCI-6259 card until the intensity reading crosses a pre-determined threshold (the value of threshold is calibrated in advance by trial and error). Upon detection of the larva the fluidic valve is switched to the water/LMP agarose reservoir. The aspiration rate is subsequently decreased to $83 \mu\text{l/s}$ to avoid damaging the larva while dispensing and forming a droplet. Consequently, the Prior X-Y stage moves the distance of a well. After 24

or 96 droplet array is formed, a temperature control module cools down the plate to 4 °C for solidifying agarose droplets. Next, the system goes into the microinjection cycle, as stated in **Section 4-3**. The high-speed CCD at the top port is continuously reading at 100 frames/second via a 5X objective lens. The zoom and focus is controlled automatically via Nikon motorized microscope. The motorized manipulator that holds the injector with in-house built automated controller brings the injection needle to the target Z position, and dispenses solutions into the larva. After injecting, the needle is moved to the original location. The system is now ready for the next cycle of operation.

4-5 Health Assessment

The syringe was operated at three different initial aspiration rates of 165, 250 and 330 $\mu\text{l s}^{-1}$ for loading 2-d.p.f. larvae from multiwell plates. In total, 450 larvae were anesthetized with 0.20 mg ml⁻¹ tricaine, loaded and dispensed from the platform. A control group of 150 larvae from the same breed were similarly anesthetized. Health assessment was based on both functional and morphological criteria measured. Functional criteria included visual confirmation of normal heartbeat and reflex response to touch stimuli. Morphology criteria included bending (that is, lordosis, kyphosis and scoliosis) and craniofacial abnormalities. Abnormalities were counted even if the zebrafish regenerated later.

Figures

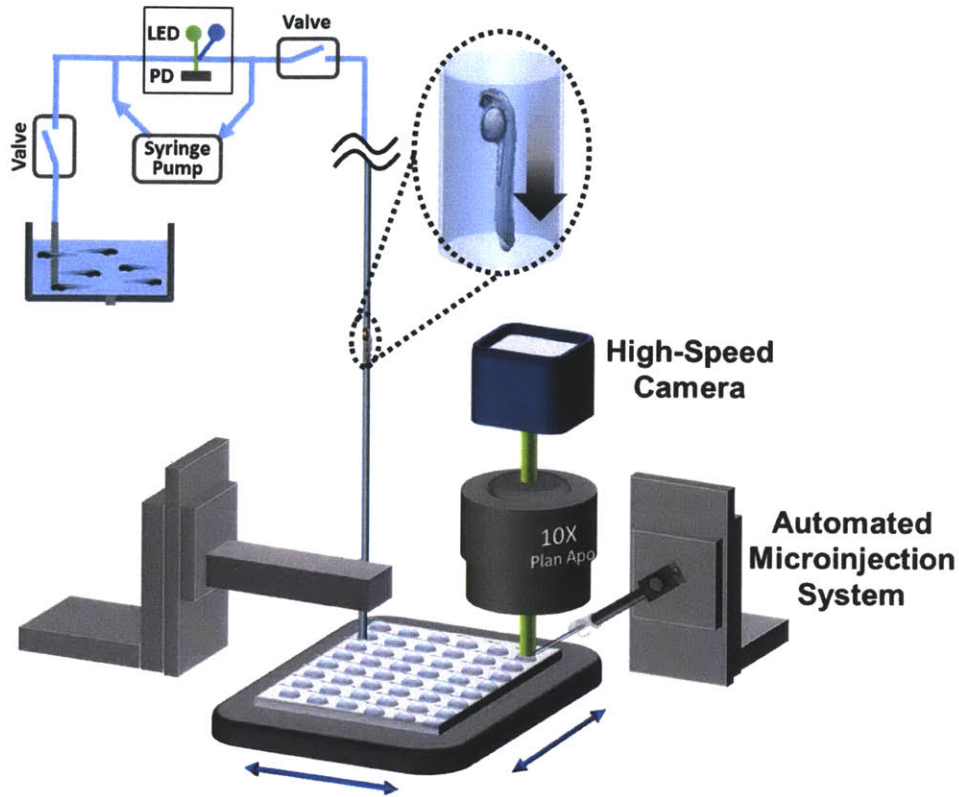


Figure 4-1. Schematic of the vertebrate automated microinjection system. Larvae immersed in liquid low-melting-point agarose are automatically loaded from a multiwell plate into the droplet arrayer and deposited onto a surface-treated plate. Both the loading and arraying plates are held on motorized x-y stages and the loading and dispensing nozzles are mounted on motorized z stages. After being arrayed in a grid, larvae are induced to assume a dorsal-up orientation by agitating the plate with a vibration motor. The agarose droplets are then cooled using a thermoelectric cooler to immobilize the larvae. The automated microinjection system automatically identifies each larva and

positions the region of interest under the injection needle. A computer-controlled microinjection module then injects test compounds into the target tissue. After injection, a self-adhesive bottomless multiwall plate is attached to the arraying plate and the larvae are recovered from the agarose droplets by gentle water flushing.

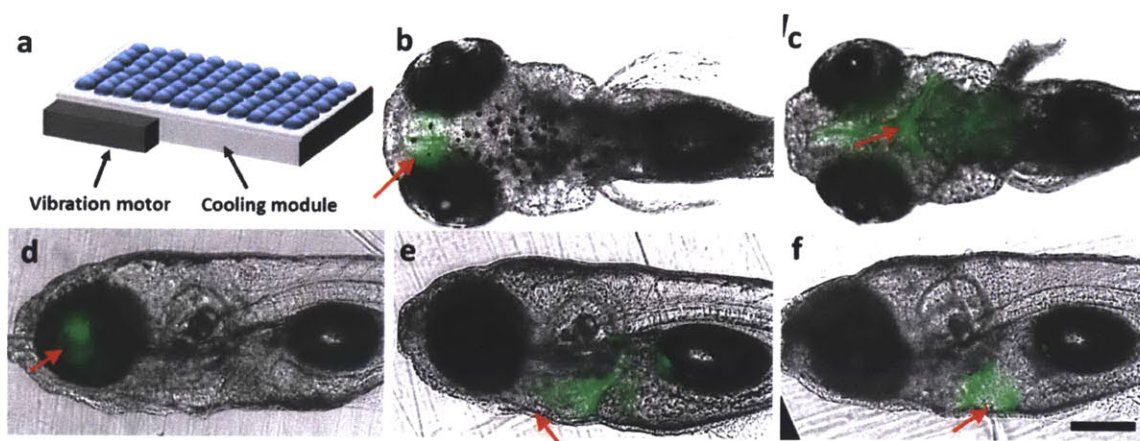


Figure 4-2. Orientation mechanisms and images of injected fish. (a) Schematic of self-orientation and immobilization setup. (b)-(f) Images of FITC coupled dextran microinjection targeting different organs. (b) Microinjection targeting the fore-brain. (c) Microinjection targeting the ventricle. (d) Microinjection targeting an eye. (e) Microinjection targeting the heart. (f) Microinjection targeting the liver. Scale bar, 100 μm .

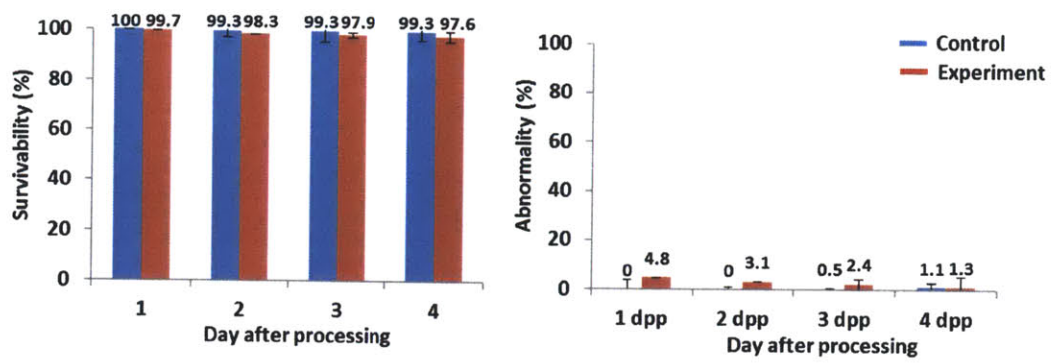


Figure 4-3. Quantitative assessment of zebrafish health after automated microinjection. (a) Survivality of larvae as a function of days post injection. ($n = 478$). (b) Abnormality of larvae as a function of days post processing (dpp). ($n = 478$)

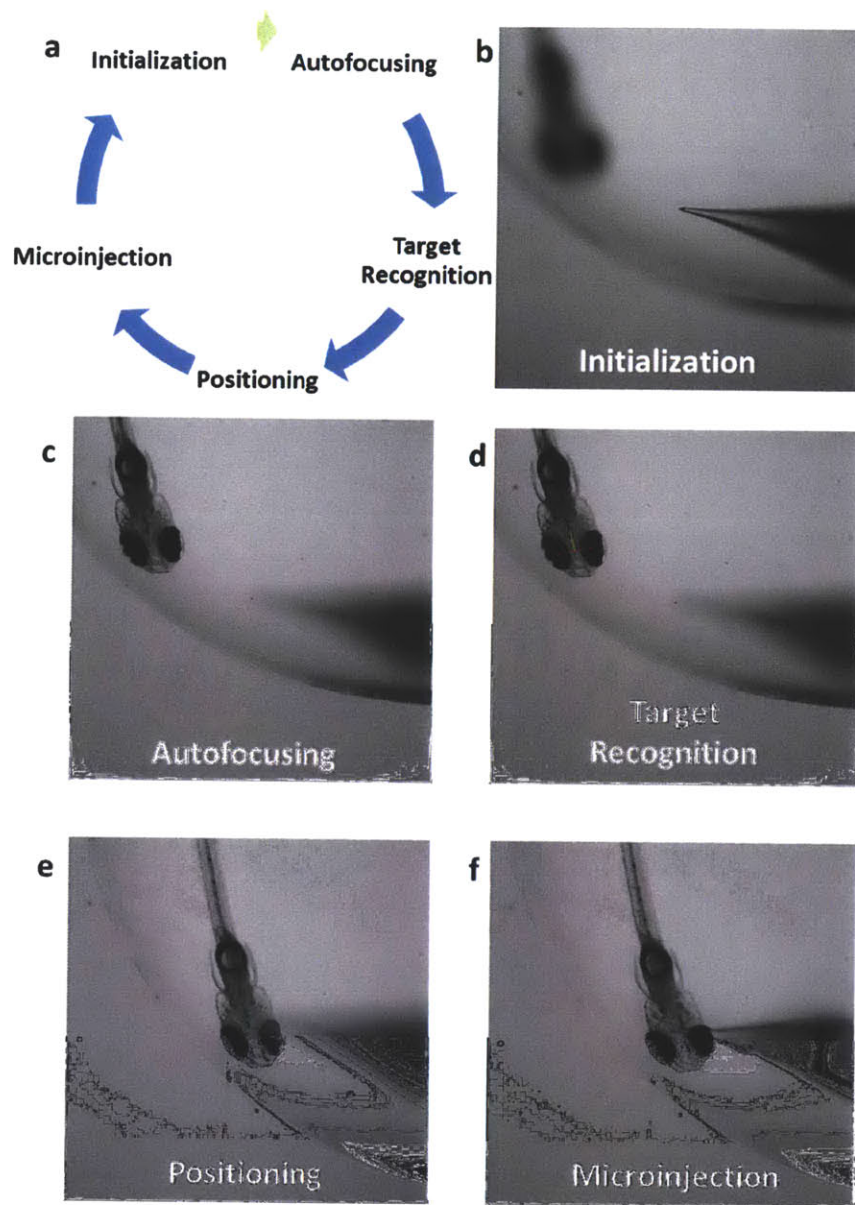


Figure 4-4. Microinjection process cycle. (a) An automated microinjection cycle consisted of five processes, including (b) initialization, (c) autofocusing, (d) target recognition, (e) positioning and (f) microinjection. In most of conditions, autofocusing does not have to be repeated every time, and therefore indicated with a green arrow.

Tables

Table 4-1. Performance of self-orientation

Orientation mechanism	Success rate ^b (%)
Dorsal orientation by stimulation	93.4 ± 2.9
Lateral orientation by anesthetization	13.6 ± 6.6
Dorsal orientation without stimulation	60.0 ± 3.2

^bn = 323

Table 4-2. Timeline of system operation

Step	Time ± s.d. ^a (sec/larva)
Loading and microdispensing	13.1 ± 0.5
Positioning	1.0 ± 0.2
Injecting	5.1 ± 0.1
Orientation and immobilization in 96-well format	0.8 ± 0.1
Overall duration for each larva in series	20.0 ± 0.9
Overall duration for each larva after pipelining	13.1 ± 0.5
Test samples front-loading	19.9 ± 6.9

^an = 60 for each

Table 4-3. Performance of automated positioning, image recognition and injection

Process	Injection Site deviation* (µm)	Time (s)	Success rate** (%)
Injection site recognition and positioning	50.1±26.4	1.0±0.1	96.0
Injection	n/a	5.0±0.1	97.3

* Ventricle is 400 µm long

** n = 75, each

References

1. Burnett, J.C. and J.J. Rossi, *RNA-Based Therapeutics: Current Progress and Future Prospects*. Chem Biol, 2012. **19**(1): p. 60-71.
2. Baum, D.A. and S.K. Silverman, *Deoxyribozymes: useful DNA catalysts in vitro and in vivo*. Cell Mol Life Sci, 2008. **65**(14): p. 2156-74.
3. Goodchild, J., *Therapeutic oligonucleotides*. Methods Mol Biol, 2011. **764**: p. 1-15.
4. Kim, S.U. and J. de Vellis, *Stem cell-based cell therapy in neurological diseases: a review*. J Neurosci Res, 2009. **87**(10): p. 2183-200.
5. Alexis, F., et al., *Nanoparticle technologies for cancer therapy*. Handb Exp Pharmacol, 2010(197): p. 55-86.
6. Lipinski, C.A., et al., *Experimental and computational approaches to estimate solubility and permeability in drug discovery and development settings*. Adv Drug Deliv Rev, 2001. **46**(1-3): p. 3-26.
7. Love, K.T., et al., *Lipid-like materials for low-dose, in vivo gene silencing*. Proc Natl Acad Sci U S A, 2010. **107**(5): p. 1864-9.
8. Falschlehner, C., et al., *High-throughput RNAi screening to dissect cellular pathways: a how-to guide*. Biotechnol J, 2010. **5**(4): p. 368-76.
9. Yang, X., N. Li, and D.G. Gorenstein, *Strategies for the discovery of therapeutic Aptamers*. Expert Opin Drug Discov, 2011. **6**(1): p. 75-87.
10. Beyer, M., et al., *A novel combinatorial approach to high-density peptide arrays*. Methods Mol Biol, 2009. **570**: p. 309-16.
11. Lieschke, G.J. and P.D. Currie, *Animal models of human disease: zebrafish swim into view*. Nat Rev Genet, 2007. **8**(5): p. 353-67.
12. Zon, L.I. and R.T. Peterson, *In vivo drug discovery in the zebrafish*. Nat Rev Drug Discov, 2005. **4**(1): p. 35-44.
13. Gutzman, J.H. and H. Sive, *Zebrafish brain ventricle injection*. J Vis Exp, 2009(26).
14. Huang, H., et al., *A universal piezo-driven ultrasonic cell microinjection system*. Biomed Microdevices, 2011. **13**(4): p. 743-52.
15. North, T.E., et al., *Prostaglandin E2 regulates vertebrate haematopoietic stem cell homeostasis*. Nature, 2007. **447**(7147): p. 1007-11.

16. Wang, W., et al., *A fully automated robotic system for microinjection of zebrafish embryos*. PLoS One, 2007. **2**(9): p. e862.
17. Chang, T.Y., et al., *Fully automated cellular-resolution vertebrate screening platform with parallel animal processing*. Lab Chip, 2012. **12**(4): p. 711-6.
18. Pardo-Martin, C., et al., *High-throughput in vivo vertebrate screening*. Nat Methods, 2010. **7**(8): p. 634-6.
19. Mueller, T., and Wullimann, M.F., *Atlas of Early Zebrafish Brain Development: A Tool for Molecular Neurogenetics*. Elsevier Science 2005.

Chapter 5

Vertebrate *in vivo* screening based on VAMP

5-1 Introduction

To demonstrate the capability of the technology, we screened a library of 59 lipid-like materials in searching for vehicles which can facilitate targeted *in vivo* delivery of therapeutic gene products [1]. This library of lipid-like materials was rapidly built using a unique synthetic strategy based on epoxide chemistry, and is composed of nondegradable amino alcohols consisting of polar amine-containing head groups and nonpolar hydrocarbon tails (lipidoids) [1, 2]. Several formulations from the library were identified to enable siRNA-directed liver gene silencing in mice at low doses [1]. In this study, the same materials are tested using our VAMP technology, in order to potentially discover vehicles that can efficiently facilitate the delivery of long protein-encoding-mRNAs into cells in the central nervous system *in vivo*. As an alternative to DNA-based gene therapy, tissue/organ targeted mRNA delivery could be a new method for delivery of therapeutic proteins [2-5], and had been a significant challenge due to mRNA's large size and susceptibility to enzymatic degradation *in vivo* [6].

5-2 *In vivo* Screening of Zebrafish and Validation

To use zebrafish larva as a predicative model for identifying most effective compound for *in vivo* mRNA delivery, lipoids in the library were complexed with mRNA encoding mCherry fluorescent protein at a constant weight ratio (10:1), and microinjected into the ventricle of each larva using VAMP. Each larva was administrated at single dose of 10 pg total mRNA. From this screen, several lipidoids were identified to facilitate *in vivo* delivery and expression of mCherry in brain tissue of zebrafish larvae (**Fig. 5-1**), which is difficult using the conventional commercially available transfection reagents. Results demonstrate the extraordinary ability of epoxide lipidoids to effectively deliver mRNA into cells in zebrafish central nervous system. Each condition was tested with more than 8 larvae and results indicate no evidence of toxic effects via health assessment [1]. The experiments follow **CAC protocol 0112-008-15 (Appendix)**.

Conservancy in Rodent Models. Next, the top three compounds screened from zebrafish model, C16-62, C16-120, C12-120, and two randomly chose compounds, C8-100, C10-62, were tested within rodents to investigate whether the gene-delivery potency of the screened materials is conserved in mammalian organisms. Single dose of mCherry-encoding mRNA (0.25 µg) formulated with these materials were stereotaxically injected into the lateral ventricle of young adult female Sprague Dawley rats (n = 3, each condition) with 10:1 lipidoid:mRNA weight ratio (**Fig. 5-2a**). Animals were allowed to

recover for 48 hours before they were sacrificed and tissue was harvested for analysis of expression of mCherry protein (see **Section 5-3**). Interestingly, all five compounds showed similar relative delivery trends in the rat lateral ventricle as they do in zebrafish larva with similar potency trend was also conserved (**Fig. 5-2b-d**), which was demonstrated by both quantitative fluorescent imaging of brain slices (**Fig. 5-2e**), and dot-blotting of proteins (see **Section 5-6**) collected from isolated tissue sections (**Fig. 5-2f**). The rodent experiments follow the **CAC protocol 1011-126-14 (Appendix)**.

Cell-based Delivery Results on Rodent Primary Neural Cells. To further investigate the delivery efficacy between in vivo and in vitro assays, selected lipidoid materials were tested in rodent primary neural cells in vitro. Primary hippocampal neurons from E18 Sprague Dawley rats were harvested (see **Section 5-4**) and plated on Poly-ornithine/Laminin coated plates. 48 hours after plating, cells transfected by complexing mCherry-encoding mRNA with lipidoid at weight ratio of 10:1 lipidoid:mRNA and incubated with cells in the presence of growth media (n = 9, each condition). Via cytotoxicity assay, selected lipidoid materials were indicated no evidence of adverse effects [1]. Results show a different trend in cell-based delivery compared to in vivo results (**Fig. 5-3**). In particular, the best-performing lipidoid C12-100 from in vitro test, showed poor delivery efficacy in our in vivo screening.

Results comparison and discussion. From in vivo zebrafish and rodent assays, similar trends of delivery efficacy can be observed. For example, the difference of delivery efficiencies from C16-62 and C12-120 in rodents and zebrafish are both statistically significant when comparing with RNA alone, and between C16-62 and C12-120. The correlation coefficient (Pearson Product-moment correlation) of the assays between rodent and zebrafish is 0.96, and the correlation between rodent and neuron culture is 0.47. These results further validate the use of zebrafish as a predictive model for mammalian animals; and further prove the great potential utility of our VAMP technology in functional in vivo screening of biologic libraries. Most surprisingly, when compared to in vivo screening in zebrafish, the in vitro, rat primary neurons yielded a different predictive pattern, Possibly suggesting the zebrafish model could be a more predictable model than in vitro assays in many situations, which also suggest the large potential VAMP can have.

5-3 Ventricle Injection in Rats

Young adult female Sprague-Dawley rats (Charles River) (<350 g) were anesthetized using isoflurane and injected at stereotaxic coordinates (-3.0 RC - 0.5 ML -15 DV mm). 10 μ l of mCherry RNA was injected at a rate of 10 μ l/min. Wound on rodents was closed and were given post-operative dosages of buprenorphine and meloxicam. 48 hours following injections animals were sacrificed and tissue was collected and slices were rapidly taken using a

Vibratome (now Leica) All animal work was carried out with the approval of MIT's Committee on Animal Care (CAC) and the Department of Comparative Medicine (DCM) as well as in accordance with local, state, and federal animal care guidelines. *Note*: this experiment was done by Peng Shi and Joseph Steinmeyer.

5-4 Rodent Primary Neural Cells

Primary neurons were harvested from E18 pups taken from timed-pregnant Sprague-Dawley rats. Cells were plated at approximately 100,000 per well of Poly-Ornithine/Laminin coated 24 well plates. Cells were cultured in media composed of 50/50 DMEM/F12, and 0.5X N2 and 0.5X B27 within Penicillin/Streptomycin for the first 36 hours before antibiotic was removed in preparation for delivery. Because the presence of antibiotics has been found to have an adverse effect on lipid-based transfection efficiencies, antibiotic was removed from the media 12 hours prior to transfections. *Note*: this experiment was done by Joseph Steinmeyer.

5-5 Lipidoids-mRNA Formulations

Lipidoid-mRNA formulations for in vivo screening were made from lipidoid, cholesterol, and a polyethylene glycol modified lipid as described [1] (15, 18). Stock solutions of lipidoid, cholesterol (MW 387, Sigma-Aldrich), and mPEG2000-DMG (MW 2660, synthesized by Alnylam) were made in absolute

ethanol at concentrations of 100, 20, and 100 mg/mL, respectively. Components were combined to yield weight fractions of 52:20:28. Ethanol mixture was then added to 200 mM sodium acetate buffer (pH 5) while stirring to spontaneously form empty liposomes. mRNA at a concentration of 0.25 mg/mL in 50 mM sodium acetate was added to empty liposomes at a weight ratio of 10:1 total lipids:mRNA and the mixture was incubated at 37 °C for 30 min. Formulations were then dialyzed against PBS in 3,500 MWCO dialysis cassettes (Pierce) for 75 min. Following buffer exchange, a sample of each formulation was used for particle characterization.

5-6 Dot-blot of Rodent Brain Tissues

After collecting tissues around the ventricle region, we go through the protein extraction process for isolation of proteins by using protein extraction kit from Millipore, and follow its protocol .

Protein detection using the dot blot protocol is similar to western blotting in that both methods allow for the identification and analysis of proteins of interest. Dot blot methodology differs from traditional western blot techniques by not separating protein samples using electrophoresis. Sample proteins are instead spotted onto membranes and hybridized with an antibody probe. Semi-quantitative measurements can be made of the spots. The procedures is shown in the following paragraph.

First, label nitrocellulose membrane using a pencil to identify protein elution fractions. Second, pipette 2 μ l from each fraction onto the membrane, allow the membrane to dry. When dry, incubate the membrane in blocking solution for 1 hour. After incubation, incubate the membrane with primary antibody solution (diluted in blocking solution), for 2 hours at room temperature. And then , wash the membrane in washing buffer (3 x 10 min). Next, incubate the membrane with secondary antibody-alkaline phosphatase enzyme conjugate solution (in blocking solution) for 1 hour, prior to wash the membrane in washing buffer for three times (10 min, each). Consequently, incubate the membrane in substrate solution, until spots are visible. Finally, stop the reaction by rinsing in distilled water, and air dry the membrane.

Figures

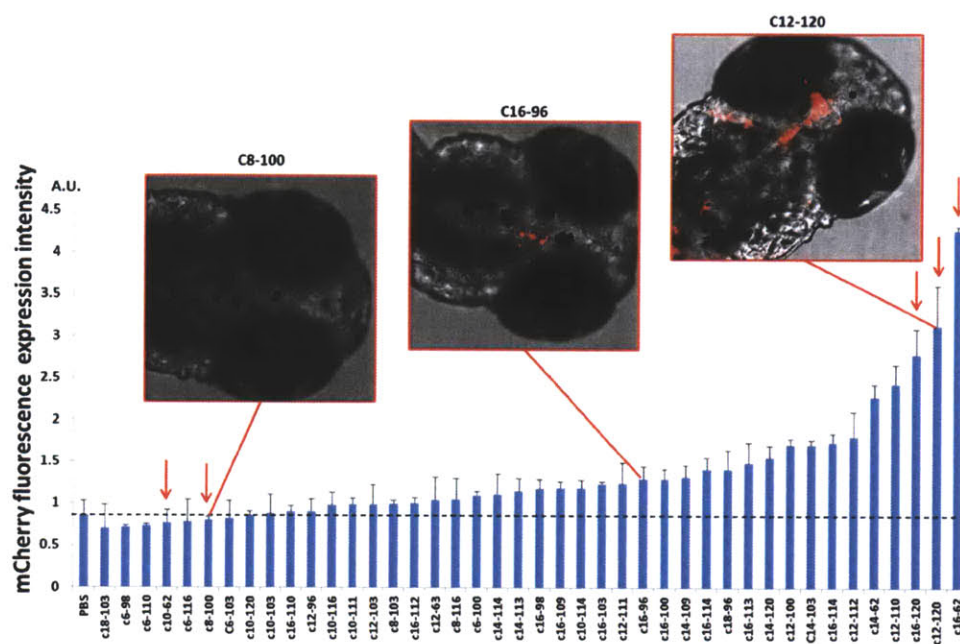


Figure 5-1. Selected in vivo screening results of lipidoid library on 4 dpf zebrafish larvae. Low dosage mCherry mRNA was complexed with lipidoids and injected into ventricles of larvae. (a) Relative expression of mRNA/lipidoids complex. Expression level is determined by mCherry fluorescence intensity. Notably, expression from C16-62 is significantly higher than from the rest of lipidoids. Red arrows indicate lipidoids for rodent assays. (n = 10, each)

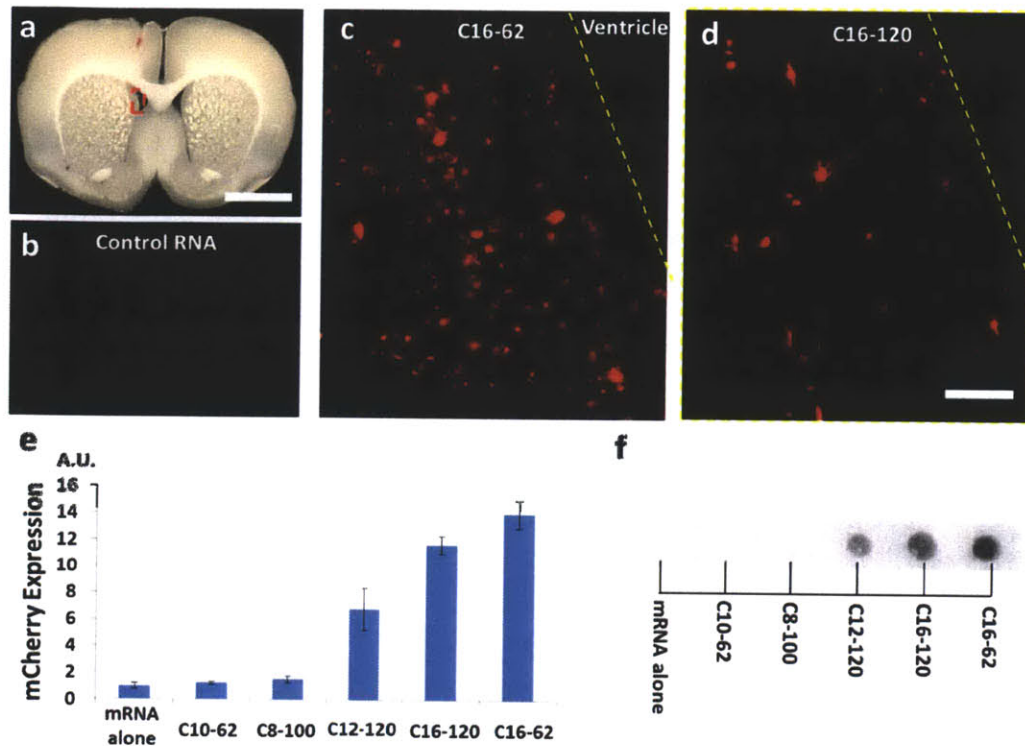


Figure 5-2. In vivo expression of mCherry-encoding mRNA with the presence of lipidoids in young adult female rats. (a) Images of a rodent brain slice. Red box circles the region to image mCherry expression and extract tissues. Scale bar, 5mm. (b)-(d) Fluorescence images of brain slices from rats with different injection materials, RNA alone, C16-62 and C16-120. Scale bar, 100 μ m. (e) mCherry expression measured by fluorescence intensity. The expression from C16-62 is significantly higher than the rest of lipidoids. (c) A representative dot-blot image shows the similar mCherry expression trends measured by fluorescence intensity. (n=3, each)

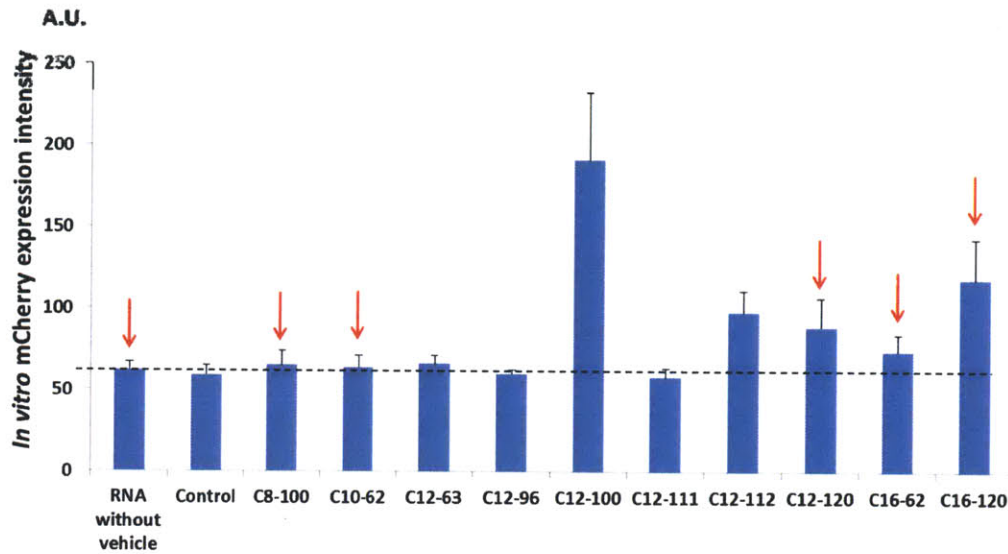


Figure 5-3. In vitro assay on rodent primary neural cells. The expression efficacy is measured by mCherry fluorescent intensity. The top three delivery compounds are C12-100, C16-120 and C12-112, which shows a different trend of delivery when compare to in vivo in zebrafish and in rodents.

References

1. Love, K.T., et al., *Lipid-like materials for low-dose, in vivo gene silencing*. Proc Natl Acad Sci U S A, 2010. **107**(5): p. 1864-9.
2. Akinc, A., et al., *A combinatorial library of lipid-like materials for delivery of RNAi therapeutics*. Nat Biotechnol, 2008. **26**(5): p. 561-9.
3. Zimmermann, T.S., et al., *RNAi-mediated gene silencing in non-human primates*. Nature, 2006. **441**(7089): p. 111-4.
4. Rozema, D.B., et al., *Dynamic PolyConjugates for targeted in vivo delivery of siRNA to hepatocytes*. Proc Natl Acad Sci U S A, 2007. **104**(32): p. 12982-7.
5. Santel, A., et al., *A novel siRNA-lipoplex technology for RNA interference in the mouse vascular endothelium*. Gene Ther, 2006. **13**(16): p. 1222-34.
6. Judge, A.D., et al., *Sequence-dependent stimulation of the mammalian innate immune response by synthetic siRNA*. Nat Biotechnol, 2005. **23**(4): p. 457-62.

Chapter 6

Conclusions

Currently, the majority of screening process starts from high-throughput *in vitro* assays and further validate via mammalian rodent models. However, validating these *in vivo* preliminary hits made by *in vitro* drug screening by mammalian animal models is significantly slow and costly, resulting in a gap in the drug development process. Furthermore, the predictability of cell-based models for advanced animal models is frequently challenged. The zebrafish is a vertebrate model organism holds a great potential to bridge this gap [1-3]. In fact, zebrafish is known as one of the most ideal animal models for *in vivo* high-throughput screening [4]. The trend of zebrafish studies is also growing exponentially.

In this Ph.D work, the author has built high-throughput screening technologies for zebrafish larvae for the first time, including Vertebrate Automated Screening Technology (VAST), Pipelining VAST and Vertebrate Automated Microinjection Platform (VAMP). A screen of the library of lipidoid compounds has been performed to validate the capability of these technologies. Furthermore, mammalian rodent experiments and *in vitro* assays have been done for examining zebrafish model as an ideal animal model for predicting advanced animal models in a high-throughput fashion.

Results of this work expand the possibility for zebrafish model to bridge cell-based assays and rodent models because of the high-throughput and low-cost advantages from our technologies as well as its high predictability for rodent models. To further unfold the capability of zebrafish model, the author suggests focusing on the following directions.

Automated microinjection for cell delivery. Delivery of cells into zebrafish holds a great potential to offer a screening model between *in vitro* and *in vivo* assays. It may unleash the possibility of new methodologies for different studies such as stem cell differentiation, cancer cell studies etc. Although some works have been done to show the advantages of cell-delivery based assays [5], cell-delivery techniques are quite challenging because of cell stickiness. Actually, delivery of cells into zebrafish is a challenge even for manual injection. Our VAMP has been shown with the great capability for soluble compound and material injection. It significantly eases the efforts researchers have to do as well as reduce the needs of knowledge and skills for microinjection. To extend the ability of VAMP, reduce the painfulness of microinjection and increase the throughput, it will be an important function VAMP could have in the future.

Connections between VAST and VAMP. Currently, the connection between VAST and VAMP is via manual transportation, which limits the power of *in vivo*-TAP technology. To achieve the goal of a highly automated *in vivo* high-throughput

screening platform, one of the key priorities is to allow VAST and VAMP connecting to each other in an automated fashion. In fact, with this technology, an unmanned *in vivo* screening platform will be expectable.

References

1. Lieschke, G.J. and P.D. Currie, *Animal models of human disease: zebrafish swim into view*. Nat Rev Genet, 2007. **8**(5): p. 353-67.
2. Rubinstein, A.L., *Zebrafish: From disease modeling to drug discovery*. Current Opinion in Drug Discovery & Development, 2003. **6**(2): p. 218-223.
3. Lam, S.H., et al., *Zebrafish whole-adult-organism chemogenomics for large-scale predictive and discovery chemical biology*. PLoS Genet, 2008. **4**(7): p. e1000121.
4. Zon, L.I. and R.T. Peterson, *In vivo drug discovery in the zebrafish*. Nat Rev Drug Discov, 2005. **4**(1): p. 35-44.
5. Jung, D.W., et al., *A novel zebrafish human tumor xenograft model validated for anti-cancer drug screening*. Mol Biosyst, 2012.